BIOMANUFACTURING OF GLIOBLASTOMA ORGANOIDS EXHIBITING HIERARCHICAL AND SPATIALLY ORGANIZED TUMOR MICROENVIRONMENT VIA TRANSDIFFERENTIATION

Seungjo Park†, Alexandra D. Avera, and Yonghyun Kim*

Department of Chemical and Biological Engineering, The University of Alabama,
Tuscaloosa, Alabama

† **Present address:** Cytiva, 170 Locke Dr, Marlborough, MA 01752

*** Corresponding author**

Mailing address:

Department of Chemical and Biological Engineering, The University of Alabama, Box 870203, Tuscaloosa, AL 35487-0203

Tel: +1 (205) 348-1729

Fax: +1 (205) 348-7558

E-mail: ykim@eng.ua.edu

Keywords:

Glioblastoma, organoid, tumor microenvironment (TME), cancer stem cell, bioreactor, transdifferentiation, dedifferentiation

Abstract

Glioblastoma (GBM) is the most aggressive type of brain tumor that originates from glioblastoma stem cells (GSCs). In the brain, GSCs are supported by a tumor microenvironment (TME) residing in the perivascular niche and the hypoxic niche. The

This article has been accepted for publication and undergone full peer review but has not been through the copyediting, typesetting, pagination and proofreading process, which may lead to differences between this version and the Version of Record. Please cite this article as doi: 10.1002/bit.28191.

GBM TME is highly heterogenous and exhibits complex cell-to-cell interactions. Three-dimensional tumorspheres cultured in stem cell-enriching media is often used as an *in vitro* model. The GBM tumorspheres retain some of the transcriptional and translational GSC features but often fails to recapitulate intertumor heterogeneity. Here, we developed a simple, matrix-free, and *in vivo*-like GBM organoids (GBOs) using patient-derived xenograft GBM lines in small-scale bioreactors. Shear stress was optimized to produce highly reproducible GBOs over 1 mm diameter within 4-5 weeks. GBOs exhibited high stemness and strong cell-to-cell interactions compared to conventional tumorsphere cultures. They displayed spatial gradients of HIF-1α positive hypoxic cores where CD133-positive cells resided and spatially heterogeneous expression of NOTCH and its ligands. We also observed a self-established, hierarchically organized, and heterogeneous TME by GBM transdifferentiation into endothelial cells, pericytes, and astrocytes. Collectively, we demonstrate the ability to biomanufacture uniformly sized GBOs that recapitulate *in vivo* GBM TME features that can serve as an improved GBM *in vitro* model.

1. Introduction

Glioblastoma (GBM) is the most common and malignant primary brain tumor with a poor prognosis (Ostrom et al., 2020). Due to its invasiveness and heterogeneity, GBM remains an almost incurable disease with existing therapies (van Linde et al., 2017). Glioblastoma stem cells (GSCs) are thought to be the origin of GBM and orchestrate the tumor microenvironment (TME) by way of suppressing immune responses, inducing angiogenesis, and differentiating into multi-lineage cells (Lathia et al., 2015). Many studies targeting GSCs have shown promising results and expanded understanding of GBM therapies (Dong et al., 2019; Emlet et al., 2014; Fan et al., 2010; Shah et al., 2019; Sherry et al., 2009; Vora et al., 2020). However, applications and reproducibility of these studies have been challenged due to hierarchically organized inter- and intratumoral heterogeneity of GBM. Development of GBM organoids (GBOs) retaining heterogeneity of GBM is crucial for reliable *in vitro* GBM models.

Patient-derived xenograft (PDX) GBM models have been appreciated as the gold standard preclinical models for the disease. The PDX model is developed by implanting dissociated primary GBM cells into animal models. These models preserve the heterogeneous GBM features and the interactions between GBM and innate surrounding brain tissues; however, variations in the orthotopic engraftment efficiency, low throughput, and long duration for tumorigenesis have been challenging (Patrizii et al., 2018). It typically takes two to 11 months to generate PDX models, which is simply too long given GBM patients' median survival is 15 months.

Three-dimensional (3D) GBM tumorspheres have been widely accepted as a good surrogate *in vitro* GBM model to the PDX models. The tumorspheres are spontaneously formed in stem cell-enriching media supplemented with basic fibroblast growth factor (bFGF) and epidermal growth factor (EGF), and they highly display stem cell-like characteristics and tumorigenesis capability (Lee et al., 2006; Zhu et al., 2011). The tumorsphere model retains a high GSC population inside the sphere, but it does not preserve cell-to-cell interactions between differentiated GBM and GSCs, which support the GSC niche and tumor growth (Wang et al., 2018). To improve upon the tumorspheres, GBM organoids (GBOs) was developed using Matrigels, together with the addition of Rho kinase (ROCK) inhibitor (ROCKi) and other mitogens (Hubert et al., 2016). In this system, GBOs were able to continuously grow up to one year and exhibit an oxygen gradient with hypoxia features. However, these GBOs were developed by aggregating different colonies in the Matrigel. Also, the growth of GBOs became stagnant after a few weeks. Recently, GBO models were further improved by adopting Lancaster's cerebral organoid culture system (Klein et al., 2020; Lancaster et al., 2013; Ogawa et al., 2018). Furthermore, a GBO culture system preserving the parental tumor features using resected patient tissues for chimeric antigen receptor (CAR) T cell therapy was established within two months (Jacob et al., 2020). However, this method requires patient samples, is not scalable, and displays various subregional sectioned clone-derived GBOs. Thus, the infusion of CAR-T cells into GBOs expressing heterogeneous antigens needs to be further studied.

Here, we report a GBO biomanufacturing method using a small-scale bioreactor. The agitation rate and media supplements were optimized. The size of the GBOs grew gradually in a controlled manner. Under the optimized culture conditions, transcriptional features of GBOs were compared with those from the conventional culture platform. Cell-to-cell interactions were analyzed by scanning electron microscope (SEM). GBOs were sectioned and immunostained to verify hierarchically and spatially organized heterogeneous GBM TME. Finally, underlying mechanisms of self-assembled GBM TME were proposed. Collectively, our study demonstrates a scalable biomanufacturing platform for producing GBOs that retain *in vivo* heterogeneity and a hierarchically self-organized GBM TME.

2. Results

2.1 Optimization of GBM Organoids (GBOs) Production

Various bioreactor vessel configurations and parameters were tested to optimize GBO culture conditions (Tables 1-2). Operating parameters were selected to maintain maximum shear stresses from 0.2 Pa to 0.4 Pa, which was previously reported to minimize shear-induced cell death (Panchalingam et al., 2010). First, we tested different bioreactor geometries: vessel diameter (*D*) over impeller diameter (*d*) with the same shear stress (0.2 Pa). The BR2 (*D/d* 1.3) promoted significantly better cell proliferation compared to the BR1 (*D/d* 1.5) and produced uniformly sized (Figures 1a and 1b). In the BR2 condition, the cell proliferation was reproducible, and the cell viability remained high (Figure 1c). With the BR2 geometries, the higher agitation rate (120 rpm) slightly improved cell proliferation (Figure 1d).

Next, we tested the effects of Rho-associated protein kinase inhibitor (ROCKi) Y-27632 on different bioreactor culture conditions. It was previously reported to enhance GBM tumorsphere formation and expansion of pluripotent stem cells (Liu et al., 2014; Tilson et al., 2015). To verify the effects, U251 was inoculated as single cells with or without ROCKi. Cells grown without ROCKi showed significantly increased cell proliferation compared to those with ROCKi (Figure 1e). To test whether low cell proliferation is a result of apoptosis, live and dead cells were stained. ROCKi did not induce apoptosis in GBO (Figure 1g). Regardless of ROCKi, the higher agitation rate (120 rpm) induced significantly higher cell proliferation compared to the lower agitation rate (60 rpm) and produced more uniformly sized GBOs (Figures 1e and 1f). This was more pronounced in the BR2 condition (*D/d* = 1.3), where the resulting power input was nearly 7-fold higher due to the higher agitation rate (Table 2). Although the BR2 with the lower agitation rate (60 rpm) did generate GBOs greater than 500 μm in diameter, these organoids were not uniform in shape and were more likely formed by random aggregations (Figure 1f). To further examine whether ROCKi maintained GSC stemness, the expression of GSC markers, SOX2 and CD44, were analyzed (Figures 1h and 1i). Regardless of the presence of ROCKi, SOX2 and CD44 were highly expressed, and their expression levels were not significantly different.

Collectively, the BR2 condition (*D/d* 1.3) with the high agitation rate (120 rpm) improved cell proliferation, prevented GBO production from random aggregations, and produced GBOs with less variation in their size. ROCKi inhibited cell proliferation in the bioreactor but did not induce apoptosis. Also, ROCKi did not alter GSC protein marker expression.

2.2 Stable Production of PDX GBOs over Millimeter Scale

It was previously shown that millimeter scale brain organoid model can drive stem cell differentiation, subsequently organizing into differentiated cell layers (Lancaster et al., 2013). Thus, GBOs of this scale may exhibit organized TME with high heterogeneity induced by GSC differentiation. To achieve millimeter-scale GBOs, U251 and PDX cell line JX6 were inoculated as single cells and continuously cultured in the bioreactor without dissociation over 30 days (Figure 2). Growth of the bioreactor GBOs (bGBOs, 120 rpm) were compared with static tissue culture flask cultured GBOs (tGBOs, 0 rpm) in terms of their size and circularity. Growth of U251 bGBOs slowed down after 3 weeks, whereas JX6 bGBOs became larger than 1 mm in diameter in 5 weeks (Figures 2d and 2e). Most U251 and JX6 tGBOs were generated by random aggregations (Figure 2a). Although the cells kept proliferating and increasing in number, the overall viability of both U251 and JX6 bGBOs gradually dropped over the culture period (Figure 2b), most likely due to the hypoxic core developed inside the bGBOs. Variations in the bGBOs' size and circularity were significantly smaller than those of tGBOs for both cell lines (Figures 2f and 2g). The high circularity indicates that the bGBOs were produced by cell proliferation, not by random aggregations. High circularity and the growth of the bGBO were not dependent on cell lines but on the bioreactor culture system (Figure 2c). Together, the large bGBOs were stably produced within 5 weeks by clonal proliferation, and JX6 showed constantly higher proliferation compared to U251.

2.3 Structural Integrity of Bioreactor-Produced GBOs by Cell-to-cell Interaction

To further investigate the GBO surface morphology in response to the shear stress of the bioreactors, tGBOs and bGBOs were imaged with SEM and compared (Figure 3). The bGBOs showed smoother surfaces and adherent cell morphology compared to tGBOs (Figures 3a and 3b). The high cell-to-cell interactions were observed even when the size of the bGBOs was smaller than 300 μm (Figure 3b). Cell-to-cell interactions were further strengthened by building bridges of lamellipodia (Figure 3b white arrows). Interestingly, cells on the bGBOs showed axon-like long protrusions of over 100 μm (Figure 3b cyan arrows). As the bGBOs grew, cell-to-cell interactions stitched over empty spaces, indicating tight junction (TJ)-mediated cell-to-cell interactions that resulted in smoother and flatter surfaces of the bGBOs (Figure 3b black arrows). This high and strong cell-to-cell interactions allowed the bGBOs to have high cell density, which mimic the dense cell population of *in vivo* GBM features.

In contrast, we observed an overall weaker cell-to-cell interactions and structural integrity in tGBOs. tGBOs greater than 1 mm in diameter were easily dissociated even with gentle media addition, and the average size of tGBOs was limited to smaller than 500 µm in diameter even when continuously culturing without dissociation. The SEM images of tGBOs also revealed that they had rough surfaces, and cavities were present (Figure 3a). Morphologically, cells in the tGBOs remained round, retained distinct individual cell shapes with vastly radiating microvilli and filopodia (Figure 3a). Thus, it appears that the sublethal constant agitation in bioreactors induced the bGBOs to acquire strong structural integrity *via* TJ-mediated cell-to-cell interactions that were absent in static tGBOs.

2.4 Secretion of Extracellular Vesicles (EVs) and Exosomes

Extracellular vesicles (EVs) were previously found to be secreted by tumor cells as a means to modulate their TME and mediate cell-to-cell communication (Nakano et al., 2015). EVs can be heterogeneous both in size and in the type of cargos depending on what they carry. It has been suggested that GSCs employ EVs for intercellular communication. Since we utilize stem cell-enriching conditions, we hypothesized that EVs would play an important role in developing GBOs (Figure 3).

Using SEM, we observed a clear formation of EVs in both tGBOs and bGBOs (Figures 3a,b). Interestingly, EVs secreted from the bGBOs were fully budded out and larger than the EVs from the tGBOs (Figure 3c yellow arrows). On the other hand, the tGBOs showed membrane ruffling and budding EVs on their surfaces (Figure 3c yellow arrows). Both GBO models secreted similar size of EVs (Figure 3d). Many exosomes, which are smaller submicron subset of EVs, were also found on the surface of both GBO models, indicating that cell-to-cell communications were also mediated by them (Figure 3c pink arrows). The exosomes from bGBOs had more variety of sizes and were larger than those from the tGBOs (Figure 3c red arrows). Interestingly, EVs were found where physical cell-to-cell connections were formed with neighboring cells in bGBOs (Figure 1c ii and 1c iii yellow box, red and pink arrows). These various sizes of exosomes secreted from the bGBOs were further verified by TEM analysis (Figures 3d,e). The sizes of the bGBO exosomes were much greater than those of the tGBO exosomes (118 ± 34 nm vs 25 ± 4 nm, respectively). Therefore, while both tGBOs and bGBOs secreted EVs, EVs from bGBOs promoted a more noteworthy formation of physical cell-to-cell interactions.

2.5 Upregulation of Transcriptional GBM Phenotypes in Size-Dependent Manner

Next, the transcriptional phenotypes of the bGBOs were analyzed as a function of size to verify whether the bGBOs maintained their stemness and heterogeneous molecular profiles as they grow (Figure 4). Gene analysis showed strong positive correlation between the size of GBOs and gene expression, as well as a strong correlation among the various genes (Figures 4a and 4b). This strong positive correlation indicates that the larger bGBOs exhibited higher stemness and heterogeneity. The gene expression sorted by duration of culture shows the strong positive correlation between the size and the gene expression was only evident by weeks 3 and 4 (Figure 4c, W3 and W4). Further gene analysis revealed that this expression pattern was grouped by three different ranges of the bGBO sizes: single cells – 400 μm diameter, 400 μm – 700 μm diameter, and greater than 700 μm diameter (Figure 4d).

The correlation between the gene expression and the GBO size was further investigated (Figure 4c). Strong positive correlation between the size and the gene expression started to emerge when the size of the bGBOs was greater than 400 μm in diameter (Figure 4e). Particularly, upregulation of *HIF-1α* suggests a new factor governing molecular profiles of the bGBOs. Recent study showed that *in vitro* tumor spheroids greater than 200 μm contain a hypoxic core (Barisam et al., 2018; Daster et al., 2017). More importantly, *in vivo* histopathological results demonstrated that the median distance between hypoxic area to the closest blood vessels is 130 μm (range, 80-200 μm) (Beasley et al., 2001). Thus, bGBOs larger than 400 μm in diameter were expected to start developing a hypoxic core, and our data corroborates with these prior studies.

To better understand the interdependent correlation among the tested genes, statistical prediction model analysis was performed (Figure 4f). Upregulation of *CD133* and *NESTIN* was highly associated with *HIF-1α* expression rather than the GBO size. Although the correlation between *VEGFA* and *HIF-1α* became positive when GBOs grew larger than 400 μm in diameter, *VEGFA* showed stronger correlation with *NOTCH1* than with *HIF-1α* in the bGBOs. This indicates that the transcription of *VEGFA* was dominantly regulated by NOTCH signaling. *HES1* and *HEY1*, downstream of NOTCH signaling, were more associated with *NOTCH1* than *NOTCH2*. Interestingly, the expression of a pericyte marker *ACTA2* was associated with *NOTCH2*, which indicates that NOTCH2 signaling may drive the GBM transdifferentiation into pericytes.

Collectively, these global gene expression analyses demonstrated that a strong correlation exists between the size of the bGBOs and their molecular profiles. Activation of stemness gene expression started when the size of the bGBOs was greater than 400 μm in diameter, mimicking the distance of diffusion limitation previously reported *in vivo*. *HIF-1α* was a key regulator governing GSC molecular profiles. The upregulation of *CD133* along with *HIF-1α* suggests that the GSCs are results of *HIF-1α* activation.

Finally, the *NOTCH* upregulation was associated with angiogenesis and transdifferentiation of GBM.

2.6 Self-Established GSC Niches

Given the global gene expression analysis (Figure 4), we hypothesized that the bGBOs with greater than 400 µm diameters start reprogramming themselves to build a heterogeneous TME *via* HIF-1α and NOTCH. To examine this hypothesis, different sizes of bGBOs were compared with tGBOs, with GBOs produced by forced cell aggregations in U-bottom well (uGBOs) and with serum-induced differentiated glioblastoma cells (DGC). Small bGBOs (smaller than 500 µm diameter) had no sign of a hypoxic core confirmed by HIF-1α or CD133-positive GSCs (Figure 5a). On the other hand, large bGBOs (greater than 800 µm diameter) displayed the development of a hypoxic core shown by HIF-1α-positive region where the cells expressed CD133. The area where CD133 expression overlapped with HIF-1α recapitulated *in vivo* histopathological features of the hypoxic niche. Large uGBOs and tGBOs also had CD133-positive cells, but their CD133-positive cells were not spatially organized and not overlapped with the HIF-1α-positive region (Figure 5b). DGCs did not express CD133 and HIF-1α proteins.

Hypoxia induces transdifferentiation of GSCs into endothelial cells for tumor vascularization (Ricci-Vitiani et al., 2011; Rocha et al., 2018). Many studies showed that CD133-positive cells exhibit endothelial cell phenotypes and co-express CD31 *in vivo* (Christensen et al., 2011; He et al., 2012; Hilbe et al., 2004). This *in vivo* GBM feature was confirmed in the bGBOs. Cells expressing CD31 resided near the CD133-positive cells, and CD133/CD31 double positive cells were observed (Figure 5c). Presence of

CD31-positive cells indicates that the bGBOs were capable of tumor vascularization and transdifferentiation into endothelial cells.

We also examined the expression of CD44, a tentative GSC marker, and its spatial variation in the bGBOs (Figure 5d). It was reported that CD44 collaborates with CD133 in GBM and is highly correlated with tumorigenesis (Brown et al., 2017). CD44 was expressed throughout the bGBOs, but its expression did not overlap with the CD133- and HIF-1α-positive expression area. Thus, CD44 expression was not likely associated with hypoxia. Distinct CD44 and CD133 singly positive cells indicated that a heterogeneous GSC population had emerged.

Another GSC marker NOTCH1 and its ligands DLL1 and DLL4 were also analyzed to further investigation of gene analysis. Large bGBOs showed doughnut-shaped gradient expression of NOTCH1 (Figure 5e). NOTCH1 expression diminished near the center of the organoids where hypoxic niche was observed (Figure 5a). This phenomenon agreed with many previous studies that showed that NOTCH is preferentially expressed near the perivascular niche where there is abundant oxygen and nutrients (Bayin et al., 2017; Charles et al., 2010; Zhu et al., 2011). Likewise, the expression of NOTCH was high near the surface of the bGBOs where mass transfer was not limited. This contrasted with the center of the GBOs where there were significant diffusion limitations. Thus, the organoids mimicked the perivascular niche found *in vivo*. NOTCH1 ligands DLL1 and DLL4 were spatially and highly expressed in the NOTCH-positive region, suggesting the activation of NOTCH signaling (Figures 5e and 5g). The tGBOs and DGCs showed poor expression of both markers (Figure 5f).

It has been reported that NOTCH-DLL signaling plays an important role in angiogenesis, and inhibition of the signaling sensitizes GBM to anti-VEGF therapy (Benedito et al., 2009; Hellstrom et al., 2007; Li et al., 2011). We therefore examined whether NOTCH-DLL signaling is spatially correlated with VEGF receptor-1 (VEGFR1) and its spatial organization (Figure 5h). VEGFR1 expression displayed a similar pattern of NOTCH1 in the large bGBOs. Interestingly, there was a clear border between vasculogenic differentiation marker CD144-positive cells and VEGFR1-positive cells. It was reported that the signaling of CD144 to VEGFR1 mediates formation of vasculogenic mimicry (VM) (Frank et al., 2011). The formation of VM in our GBOs was verified by the co-expression of CD144 with CD146 and MAP2 (Figure 5i). Thus, CD144-mediated VM formation in the large bGBOs can be a potential *in vitro* model for tumor vascularization. In contrast, the uGBOs and the tGBOs did not show clear spatial expression of VEGFR and CD144 (Figure 5j).

Taken together, our bGBOs mimicked the *in vivo* spatial organization of GBM, namely the hypoxic niche and the perivascular niche. VEGFR1 expression was highly associated with NOTCH1 expression pattern, which was consistent with the gene expression analysis. We also confirmed the transdifferentiation of GBM into endothelial cell phenotypes and formation of VM supported by pericyte and astrocyte. Size-dependent spatial expression and transdifferentiation can be the result of GSC plasticity, which recapitulates heterogeneous *in vivo* GBM TME features.

2.7 Establishment of GBM TME Driven by Transdifferentiation of GBM into Endothelial Cells, Pericytes, and Astrocytes

Global gene expression analysis of our GBOs above revealed that the transdifferentiation of GBM into pericytes was regulated by increased *NOTCH* expression (Figure 4) and that cells transdifferentiated into endothelial cells (Figure 5). The transdifferentiated cells may play a role in establishing heterogenous GBM TME, and thus, the presence of transdifferentiated GBM and their spatial distribution were further analyzed. To investigate transdifferentiation, IHC analysis of GBOs was performed with endothelial cell markers (CD34 and CD144), pericyte markers (α-SMA [ACTA2], NG2, and CD146), and astrocyte markers (S100B, MAP2, and GFAP). In the large bGBOs (greater than 800 µm diameter), α-SMA expression showed the most distinctive spatial variation, encircling the core region where hypoxia was present (Figure 6a). In contrast, α-SMA was not expressed in the small bGBOs (smaller than 500 µm diameter), which agreed with our prior gene analysis. The cells expressing α-SMA had an elongated morphology, similar to DGCs' morphology (Figure 6b). The uGBOs had only a few cells expressing α-SMA and showed no patterns of spatial organization, whereas the tGBOs showed poor expression of α-SMA (Figure 6b). Other pericyte markers (i.e., NG2 and CD146) also did not display spatial expression in the small bGBOs (Figures 6c and 6e). NG2 expression was poor in the uGBOs and the tGBOs compared to bGBOs. Particularly, the tGBOs did not show any NG2 expression.

The large bGBOs was strongly positive for CD34 and CD144 cells near the core region (Figures 6b and 6e). The expression of CD34 and CD144 was not induced by serum (Figures 6b and 6f). Interestingly, CD146/CD144 double positive cells were also observed in the large bGBOs (Figure 6e). This corroborated with other studies that showed that endothelial progenitors share pericyte and endothelial cell markers (Desai et al., 2009; Hristov et al., 2003; Park et al., 2020; Timmermans et al., 2009). Thus, both CD146- and CD144-positive cells may represent endothelial progenitors.

Astrocyte markers GFAP, S100B and MAP2 also showed spatially gradient expression. As GBM is a grade IV astrocytoma, the expression of these markers is natural. However, the gradient expression of these markers with the size increase of the bGBOs indicates the process of spatial organization.

Collectively, the millimeter scale bGBOs featured spatially organized and transdifferentiated GBM cells. Protein expression and spatial variation became clear in the larger size GBOs. Although endothelial cell markers expression was not as clear as some of the other markers, the expression levels of endothelial cell markers were significantly higher than those of tGBOs and DGCs.

2.8 Hierarchically and Spatially Organized GSC Niche with Tumor Necrotic Region

A necrotic area is a common histopathological GBM feature and governs signaling pathways in the GBM TME (Ahn et al., 2016; Liu et al., 2017; Rong et al., 2006). Necrotic regions commonly accompanied with a hypoxic environment create inflammatory microenvironment. For example, TNF-α induces TGF-β, which subsequently can further induce α-SMA expression (Desmouliere et al., 1993; Hu et al., 2003; Warshamana et al., 2001; Yoshimatsu et al., 2020). To model these necrotic environmental features, bGBOs larger than 1.5 mm in diameter were characterized.

These bGBOs greater than 1.5 mm diameter exhibited a large necrotic core (NC) near the center where lots of DNA fragments were observed (Figure 7). In addition to the

NC, formation of VM was confirmed by shape and high expression of α-SMA, CD144, and CD31 on the border of the labeled region (Figure 7a, VM). Spheroid shape of distinctive GBM TME was localized near the NC (Figure 7 HN; hypoxic niche). This area exhibited a high expression of CD133, VEGFR1, GFAP, and MAP2. The expression of CD133 accompanied with the high and distinctive spatial expression of VEGFR1 suggested a potential GSC niche possessing angiogenesis feature. Some CD31-, CD34-, and CD144-positive cells were found in the HN area; however, these markers were more expressed around the circled area, which may play roles in supporting CD133-positive cells (Figure 7d). The HN area suggests a potential GSC niche accompanied with endothelial cells supporting GSC niche.

NOTCH1 expression was poor in the hypoxic niche, but we found another potential perivascular niche model where NOTCH1 expression was high (Figure 7e, PVN). In this area, cells expressing NOTCH1 also formed a spheroid shaped colony like the potential hypoxic niche. This perivascular niche was within 200 μm from the surface of the bGBOs where there are enough oxygen and nutrients. This gradient expression of NOTCH1 was confirmed again, which agrees with Figure 5e, indicating reproducible and spatially organized heterogenous GBO models.

α-SMA displayed the most distinctive spatial expression (Figure 7a). Expression of α-SMA was high along the necrotic core. This spatial expression of α-SMA can be the result of cytokines released in an inflammatory environment due to the necrotic core. Interestingly, the potential GSC hypoxic niche was devoid of α-SMA (Figure 7a). Thus, it is most likely that cells expressing α-SMA were fully differentiated. NG2 expression also diminished in the HN region. However, this area was strongly positive for S100B and MAP2. The distinctive spatial expression of astrocytes and pericytes indicates established GBM TME supported by fully differentiated cells.

Together, the necrotic GBM TME shows multiple hierarchically and spatially organized GSC niches. These GSC niches were identified by distinct areas of CD133- and NOTCH1-positive cells. Notably, the niches were void of pericyte and endothelial cell markers. The hierarchical organization was highlighted by pericytes near the necrotic core and endothelial cells surrounding the CD133-positive GSC niche area.

2.9 Self-Assembled GBM TME Driven by High Cell-to-Cell Interactions and Activation of POU3f2 and HIF-1α

bGBOs exhibited strong and physical cell-to-cell interactions supported by TJs (Figure 3). Therefore, we hypothesized that the regulation of cell-to-cell interactions mediates spatial organization of GBM TME. TJ plays important roles in intercellular interactions, invasion, and blood-brain barrier permeability (Bhat et al., 2019). TJ not only mediates differentiation and proliferation but also plays a role in maintaining the integrity of organoid models and stemness (Matter et al., 2005; Xing et al., 2020; Xu et al., 2012).

To examine our hypothesis, different sizes of the bGBOs were stained by ZO-1, a TJ protein (Figure 8a). Cells having an elongated morphology were actively migrating in the center region of the bGBOs when they were greater than 500 μm in diameter containing a hypoxic core as shown in Figure 5. It was reported that hypoxia decreases expression of TJ and allows the cells to have high mobility (Luo et al., 2018). Thus, the highly elongated cells displaying lower ZO-1 expression can be in response to the hypoxic TME. In contrast in larger bGBOs, ZO-1 was highly expressed on the boundary of the small necrotic regions, which allows for clear internal structure of the bGBOs (Figure 8b). The formation of TJ along the necrotic areas may protect the cells from acidic and hypoxic environmental factors including inflammatory cytokines which cause apoptosis. Interestingly, the potential hypoxic niche shown in Figure 7 highly expressed ZO-1 but not CD31 (Figure 8c). It was reported that ZO-1 expression decreased during metastasis, but cancer cells recover ZO-1 expression in metastasized site (Kaihara et al., 2003). Also, ZO-1 knockout stem cells failed to form spheroids *in vitro* (Xing et al., 2020). Therefore, the spheroid shape of the potential hypoxic niche and the high expression of ZO-1 provide evidence of a newly and hierarchically established GSC niche in our bGBOs.

GSCs in their niche can be differentiated or dedifferentiated by activation of transcription factors. POU3f2, SALL2, and HIF-1α have been reported to induce dedifferentiation of GSCs (Lee et al., 2016; Suva et al., 2014). To better understand the underlying mechanisms of CD133-positive cells shown in Figure 7, expression of POU3f2, SALL2, and HIF-1α was examined. In the hypoxic niche, cells highly expressed the three transcription factors, suggesting that CD133 expression was maintained by POU3f2, SALL2, and HIF-1α.

Collectively, we propose that the establishment of the GSC niche in the bGBOs was driven by cell-to-cell interactions and activation of transcription factors involved in GSC dedifferentiation (Figure 9). Spatial organization was initiated by downregulating ZO-1 near the center. Near the necrotic regions, the expression of ZO-1 was high and may protect cells from the inflammatory factors and acidic TME. In our bGBO model, the hypoxic niche was spatially and hierarchically organized by activation of POU3f2, SALL2, and HIF-1α.

3. Discussion

In this study, we employed a small scale, matrix-free stirred tank bioreactor for an accelerated GBO production. Production of bGBOs with greater than 1 mm diameter was achieved within just five weeks. The bGBOs were produced with uniform sizes and without random clonal aggregations.

SEM image analysis of bGBOs showed strong cell-to-cell communications *via* physical interactions and secretion of EVs. EVs and their effects on cell proliferation and differentiation needs to be further characterized and studied in the future. Heterogeneous size of EVs released from bGBO were observed on cell surface and highly involved in cell-to-cell interactions. These EVs can carry oncogenic EGFRvIII, and their effects can vary depending on the size of EVs and culture condition (Choi et al., 2018). Thus, inhibition of cell-to-cell communication *via* EVs can be a potential therapeutic target.

Global gene analysis revealed that our bGBOs displayed high stemness and capability to differentiate. The gene analysis further showed that the expression of stemness genes were correlated with *HIF-1α* upregulation rather than with the size of the bGBOs. Upregulation of *NOTCH* was associated with regulating angiogenesis and differentiation. However, signaling crosstalk and other signaling pathways need to be further studied. For example, various NOTCH ligands can subsequently transduce signals and transcript multiple genes (D'Souza et al., 2008; Lino et al., 2010; Stockhausen et al., 2010; Xiu et al., 2020). To better understand the heterogeneity of molecular profiles, single cell RNA-sequencing analysis would be helpful. A recent study demonstrated a hierarchically organized GBM roadmap by single cell RNA-sequencing and demonstrated that the cells with GSC phenotypes drive chemoresistance and GBM growth (Couturier et al., 2020). Therefore, single cell transcriptome analysis can map hierarchically organized heterogeneous bGBOs.

IHC staining revealed size-dependent and self-organized GBM TME. Development of a hypoxic core and differentiation were correlated with gene transcript analysis results. Our results also showed that GBM transdifferentiated into multiple lineages and built their own GBM TME (Figure 9). In particular, transdifferentiation of endothelial cells was mainly induced in our bGBOs. The large bGBOs with necrotic regions demonstrated a hierarchically organized GBM TME. The distinctive GSC niche displayed high angiogenesis, cell-to-cell interactions, and activation of transcription factors that are involved in GSC dedifferentiation and stemness. Although we demonstrated establishment of TME by multiple GBM cells, the effects of cytokines and chemokines from necrotic regions need to be further investigated. Cytokines and chemokines in GBM TME were previously shown to transform immune cells, resulting in promoting GSC survival from immune surveillance and contributing to poor prognosis (Brown et al., 2018; Zhu et al., 2012). Understanding the cell-to-cell communication *via* cytokines and chemokines will be critical to develop cell therapy using chimeric antigen receptor T (CAR-T) cells and regulatory T cells in the future.

In conclusion, PDX bGBO models were biomanufactured in a well-controlled manner. The bGBOs were produced from single cells, and they self-established their own GBM TME that recapitulated the heterogeneous *in vivo* GBM features. Our GBO model can potentially be highly predictive *in vitro* models for preclinical study. Our GBO model can also be useful for applications such as drug screening, cell therapies, and co-culture models in the future.

4. Materials and Methods

4.1 Cell Culture

Patient-derived xenograft (PDX) GBM cell line JX6 was kindly provided by Dr. Yancey Gillespie (The University of Alabama at Birmingham). JX6 is classical subtype and characterized by amplified variant III EGFR mutation in EGFR, wild type of PTEN and TP53, and unmethylated MGMT. U87 and U251 were purchased from ATCC. Cells were cultured in neurobasal A medium supplemented with 1X GlutaMax (Gibco, 35050-061), 0.5X B-27(Gibco, 12-587-010), 20 ng/mL EGF (Shenandoah, 10026), 20 ng/mL bFGF (Shenandoah, 100-146), 8 µg/mL heparin (Akron, AK3004-1000), 1X penicillin/streptomycin (Corning, 30-002-CI), and 2.5 µg/mL amphotericin B (Cytiva, SV30078.01) (NBE). Cells were seeded at a density of 1 x 10^5 cells/mL in standard tissue culture flasks, U-bottom well plates (Greiner, 650970), and 100 mL bioreactors (Chemglass, CLS-1450-100) and incubated at 37 °C with 5% CO_2. GBOs were dissociated by incubating with Accutase (Corning, 25-058_CI) at 37 °C for 5 minutes followed by trituration to count cells. For continuous culture, GBOs were gently fed with 30 mL of media and passaged without dissociation for both tissue culture flask and bioreactor conditions. For GBOs in U-bottom well plate, 50% of the total volume of well was replaced with fresh NBE, with care given to not disturb the existing GBOs.

4.2 Bioreactor Culture System

Indented bottom spinner flasks with internal paddle impellers were used as small-scale bioreactors (Chemglass CL2-1450-100). The impellers and the inner surface of the bioreactors were coated using Sigmacote (Millipore Sigma, SL2) before cell inoculation. Sigmacoate was applied to the inside of the bioreactor walls and impellers to minimize cell damage from wall collision and to prevent cells from being trapped in between the impeller parts. A membrane filter cap on the side of the bioreactor was used for oxygen supply. The ratio of the distance between the impeller and the baffle on the bottom was maintained at 0.15. Every 5 days, GBOs were transferred to a new bioreactor to prevent fouling. As different types of bioreactor design and impellers manipulate shear stress dynamics, two different geometries of bioreactors were used to estimate shear stress and optimize culture conditions (Figure 1a). Given the bioreactor geometries, shear stress was estimated using the following equation (Cherry & Kwon, 1990),

$$\tau_{max} = 5.33\rho(\epsilon\nu)^{\frac{1}{2}}(1)$$

where ρ is the density of the medium and ν is the kinematic viscosity of the culture medium. The viscous power dissipated per mass $\boldsymbol{\epsilon}$ is determined by

$$\epsilon = \frac{N_{P0}N^3D_a^5}{V_L}(2)$$

where N_{P0} is the dimensionless power number, N is the agitation rate, D_a is the impeller diameter, and V_L is medium volume respectively. The dimensionless power number correlates with types of impeller and baffles. The dimensionless power number was calculated by using the Kamei correlation (Furukawa et al., 2012),

$$N_{P0} = \left\{\frac{1.2\pi^4\beta^2}{8d^3(D^2H)}\right\}f(3)$$

where β is the constant value from bioreactor dimension, d is the impeller diameter, D is the bioreactor inner diameter, and H is the working volume height, and f is the friction factor respectively. All equations for each parameter are in Table 1 shows the calculated parameters including eddies scale, impeller tip speed, and power input per volume (P/V).

High ratio of C/H (where C is the distance between the impeller and the bottom wall of the bioreactor) fails to generate homogeneous shear profiles in the bioreactor (Ismadi et al., 2014). C/H greater than 0.5 have the maximum shear stress at the wall of the bioreactor and the edges of the impellers (Ismadi et al., 2014). Thus, the C/H was maintained lower than 0.5 to have homogeneous shear profiles (Table 1).

Different dimensions of impellers not only generate various mixing profiles, but also are highly correlated with the power number (Furukawa et al., 2012). Two different ratios of the vessel diameter to the impeller diameter (D/d) were adopted to generate a high power number (Table 2). Even with the similar estimated shear stresses, the BR2 had a higher power consumption (1.14×10^{-4} W) than that of BR1 (9.31×10^{-5} W) (Table 2).

4.3 Gene Expression Analysis

RNA was extracted without dissociation of GBOs according to the manufacturer's protocol (GeneJet RNA Purification Kit, K0731). cDNA was prepared using the kit (RevertAid First Strand cDNA synthesis Kit, K1622) and followed the manufacturer's protocol. Gene expression was quantified by qRT-PCR (StepOnePlus, Applied Biosystems) using SYBR Green (Applied Biosystems, A25742). The following genes were tested: angiogenesis (*VEGFA*), epithelial-mesenchymal transition (*SNAI1*, *SNAI2*, *TWIST1*, and *TWIST2*), stemness (*CD133*, *SOX2, MET, NESTIN*, and *OCT4*), metabolite (*IDH1*), hypoxia (*HIF-1α*, *EPAS1*, and *ARNT*), NOTCH signaling (*NOTCH1*, *NOTCH2*, *NOTCH3*, *HES1*, and *HEY1*), and pericyte (*ACTA2*). Relative expression level of genes of interest was normalized to *GAPDH*.

4.4 Scanning Electron Microscopy (SEM)

GBOs were fixed using 2.5% glutaraldehyde in H_2O (Millipore Sigma, G5882) for an hour at room temperature and then gradually dehydrated using ethanol (50%, 70%, 95%, and 100%) for 5 min per each concentration followed by critical point drying using CO_2 over 35 °C at 1,2000 psi. GBOs then were sputter coated with 20 nm of Au and observed by Apreo FE SEM (Thermo Scientific).

4.5 Live and Dead Cell Analysis

Cells were stained with Live and Dead Cell Kit according to manufacturer's protocol (Abcam, ab115347). Sample images were acquired and analyzed using Nikon C2 Laser Scanning Confocal Microscope.

4.6 Isolation and characterization of Extracellular Vesicles (EVs)

Extracellular vesicles (EVs) were collected by sequential centrifugation: 300 x *g* for 5 min, 1,000 x *g* for 5 min, 4,000 x *g* for 10 min, 20,000 x *g* for 20 min, and 100,000 x *g* for 60 min. Supernatants were collected between each step. After 100,000 x *g* centrifugation, supernatants were discarded, and the pellet was collected for image analysis. Collected EVs were transferred to the coated formvar grid. EVs were negatively stained using 2% uranyl acetate for 10 sec and washed by adding drops of dH_2O, and the grids were air dried for 30 min. EVs images were acquired using Hitachi H-7650 Transmission Electron Microscope (TEM). Size of EVs were measured by using dynamic light scattering.

4.7 Immunohistochemistry (IHC)

GBOs were fixed using 4% paraformaldehyde (Alfa Aesar, J61899AK) overnight and dehydrated using ethanol followed by xylene. Dehydrated GBOs were embedded in paraffin. Paraffin-embedded GBOs were sectioned to 5 to 10 μm thickness. Deparaffinization was done by xylene followed by ethanol. Sectioned GBOs were rehydrated with water. 10 mM sodium citrate buffer with 0.05X Tween 20 was formulated for antigen retrieval and adjusted to pH 6.0. Antigen retrieval was performed at 95 °C for 10 min. Sectioned GBOs were stained with primary antibodies: CD133, SOX2, CD44, NOTCH1, DLL1, HIF-1α, CD31, CD34, CD144, CD146, α-SMA, NG2, GFAP, Map2, S100B, VEGFR, ZO1, and POU3f2, followed by secondary staining. Cell nuclei were counter stained by Hoechst 33342 (Invitrogen, H1399). Stained GBOs were mounted using ProLong Glass Antifade Mountant with NucBlue (Invitrogen, P36981) and imaged by Nikon C2 Laser Scanning Confocal Microscope.

4.8 Image Analysis

Colony dimensions were measured using an automated counting macro developed in-house using ImageJ (Version 1.52r, NIH). Briefly, the macro included the following process. Scale bars in each image were calibrated, and images were auto-corrected for brightness and contrast, despeckled, closed-and-filled holes, outlier removed, and watershed to clearly segregate colony lines and exclude non-whole colonies on the edges of the fields of view. We then measured the area, standard deviation, perimeter, and Feret's diameter of the colonies using the ImageJ's built-in features. The region of interest (ROI) manager was set to show all ROIs with labels. Finally, the images underwent particle analysis to show the overlay and outlines, results, summary, exclude on edges, and ensuring all ROIs were added to the ROI manager. Circularity was calculated using

$$\mathrm{Circularity} = 4\pi A/p^2 (4)$$

where A is the two-dimensional projected area, and p is perimeter. Images were acquired with 12-bit depth, and the raw files were analyzed using NIS-Elements Viewer (Nikon) and ImageJ. Fluorescence intensity was calculated by the corrected total cell fluorescence (CTCF).

Protein expression from IHC images were quantified through an object detection analysis followed by intensity profile (IP) analysis. Object detection analysis was utilized to denoise images of background fluorescence and determine the mean fluorescent intensity of target proteins with DAPI (nuclear) expression. Next, IP data was acquired by drawing a vector across the diameter, through the center of the GBO of interest within the protein expression region of interest. Details about normalization of data can be seen in the statistical analysis section. The core of the GBO was defined as 0.0 ± 0.05 of the normalized distance (i.e., 10% of the radial distance from the center). The periphery of the GBO was defined as the region outside the core region.

4.9 Statistical Analysis

Gene expressions were statistically analyzed by Pearson correlation coefficient and one-way ANOVA using Minitab 19 and JMP Pro 15.0.0. Each gene's relative gene expression was normalized to the maximum expression level of each gene and described as 'Z.' Multivariate analysis was performed to analyze principal components with the default estimation method using the Correlations option. Principal component analysis (PCA) was also performed using relative gene expression of genes of interest, the size of

GBO, and the agitation rates. Top two highest eigenvalues were chosen for the principal components. PCA was plotted using the coefficients in the principal components' formula. Significant difference among samples was analyzed by Tukey and Dunnett test. Statistical significance was assigned at p-value < 0.05.

IHC protein expressions were statistically analyzed by using the ordinary one-way ANOVA followed by the Tukey's multiple comparison tests (GraphPad Prism, v9.0). Because GBOs varied in size across samples, the distance of the IP vector was normalized to the maximum IP vector distance for each sample, such that 0.0 indicates the center of the GBO and ± 0.5 indicates opposite edges of the GBOs in radial direction. Non-cellular fluorescence (i.e., background fluorescence) from IHC images were identified and excluded from further analysis via object detection analysis for the mean fluorescent intensity of individual cells expressing DAPI and the target protein. The total number of cells along the IP vector was determined by counting the total number data points in which DAPI fluorescence was greater than zero. Normalized intensity per cells refers to the fluorescent intensity of the target protein normalized to its maximum intensity divided by the total number of cells for each sample.

Acknowledgements

This work was supported by the National Science Foundation (CBET/EBMS #2000053 to Y.K.). A.D.A. was supported by the U.S. Department of Education as a GAANN Fellow (P200A210069). Any opinions, findings, and conclusions or recommendations expressed in this material are those of the authors and do not necessarily reflect the views of the National Science Foundation. The authors also thank Dr. Yancey Gillespie (University of Alabama at Birmingham) for providing the JX6 PDX

GBM cell line and Dr. Kim Lackey (The University of Alabama) for assistance with the confocal microscopy. *S.D.G.*

Conflict of Interests

The authors declare that there is no conflict of interests.

References

Ahn, S. H., Park, H., Ahn, Y. H., Kim, S., Cho, M. S., Kang, J. L., & Choi, Y. H. (2016). Necrotic cells influence migration and invasion of glioblastoma via NF-kappa B/AP-1-mediated IL-8 regulation. *Scientific Reports*, *6*. https://doi.org/10.1038/srep24552

Barisam, M., Saidi, M. S., Kashaninejad, N., & Nguyen, N. T. (2018). Prediction of Necrotic Core and Hypoxic Zone of Multicellular Spheroids in a Microbioreactor with a U-Shaped Barrier. *Micromachines*, *9*(3). https://doi.org/10.3390/mi9030094

Bayin, N. S., Frenster, J. D., Sen, R., Si, S., Modrek, A. S., Galifianakis, N.,... Placantonakis, D. G. (2017). Notch signaling regulates metabolic heterogeneity in glioblastoma stem cells. *Oncotarget*, *8*(39), 64932-64953. https://doi.org/10.18632/oncotarget.18117

Beasley, N. J. P., Wykoff, C. C., Watson, P. H., Leek, R., Turley, H., Gatter, K.,... Harris, A. L. (2001). Carbonic anhydrase IX, an endogenous hypoxia marker, expression in head and neck squamous cell carcinoma and its relationship to hypoxia, necrosis, and microvessel density. *Cancer Res*, *61*(13), 5262-5267.

Benedito, R., Roca, C., Sorensen, I., Adams, S., Gossler, A., Fruttiger, M., & Adams, R. H. (2009). The Notch Ligands Dll4 and Jagged1 Have Opposing Effects on Angiogenesis. *Cell*, *137*(6), 1124-1135. https://doi.org/10.1016/j.cell.2009.03.025

Bhat, A. A., Uppada, S., Achkar, I. W., Hashem, S., Yadav, S. K., Shanmugakonar, M.,... Uddin, S. (2019). Tight Junction Proteins and Signaling Pathways in Cancer and Inflammation: A Functional Crosstalk. *Front Physiol*, *9*. https://doi.org/10.3389/fphys.2018.01942

Brown, D. V., Filiz, G., Daniel, P. M., Hollande, F., Dworkin, S., Amiridis, S.,... Mantamadiotis, T. (2017). Expression of CD133 and CD44 in glioblastoma stem cells correlates with cell proliferation, phenotype stability and intra-tumor heterogeneity. *PLoS One*, *12*(2). https://doi.org/10.1371/journal.pone.0172791

Brown, N. F., Carter, T. J., Ottaviani, D., & Mulholland, P. (2018). Harnessing the immune system in glioblastoma. *British Journal of Cancer*, *119*(10), 1171-1181. https://doi.org/10.1038/s41416-018-0258-8

Charles, N., Ozawa, T., Squatrito, M., Bleau, A. M., Brennan, C. W., Hambardzumyan, D., & Holland, E. C. (2010). Perivascular Nitric Oxide Activates Notch Signaling and Promotes Stem-like Character in PDGF-Induced Glioma Cells. *Cell Stem Cell*, *6*(2), 141-152. https://doi.org/10.1016/j.stem.2010.01.001

Cherry, R. S., & Kwon, K. Y. (1990). Transient Shear Stresses on a Suspension Cell in Turbulence. *Biotechnol Bioeng*, *36*(6), 563-571. https://doi.org/10.1002/bit.260360603

Choi, D., Montermini, L., Kim, D. K., Meehan, B., Roth, F. P., & Rak, J. (2018). The Impact of Oncogenic EGFRvIII on the Proteome of Extracellular Vesicles Released from Glioblastoma Cells. *Molecular & Cellular Proteomics*, *17*(10), 1948-1964. https://doi.org/10.1074/mcp.RA118.000644

Christensen, K., Schroder, H. D., & Kristensen, B. W. (2011). CD133(+) niches and single cells in glioblastoma have different phenotypes. *J Neurooncol*, *104*(1), 129-143. https://doi.org/10.1007/s11060-010-0488-y

Couturier, C. P., Ayyadhury, S., Le, P. U., Nadaf, J., Monlong, J., Riva, G.,... Petrecca, K. (2020). Single-cell RNA-seq reveals that glioblastoma recapitulates a normal neurodevelopmental hierarchy. *Nature Communications*, *11*(1). https://doi.org/10.1038/s41467-020-17186-5

D'Souza, B., Miyamoto, A., & Weinmaster, G. (2008). The many facets of Notch ligands. *Oncogene*, *27*(38), 5148-5167. https://doi.org/10.1038/onc.2008.229

Daster, S., Amatruda, N., Calabrese, D., Ivanek, R., Turrini, E., Droeser, R. A.,... Muraro, M. G. (2017). Induction of hypoxia and necrosis in multicellular tumor spheroids is associated with resistance to chemotherapy treatment. *Oncotarget*, *8*(1), 1725-1736. https://doi.org/10.18632/oncotarget.13857

Desai, A., Glaser, A., Liu, D. L., Raghavachari, N., Blum, A., Zalos, G.,... Cannon, R. O. (2009). Microarray-Based Characterization of a Colony Assay Used to Investigate Endothelial Progenitor Cells and Relevance to Endothelial Function in Humans. *Arteriosclerosis Thrombosis and Vascular Biology*, *29*(1), 121-127. https://doi.org/10.1161/Atvbaha.108.174573

Desmouliere, A., Geinoz, A., Gabbiani, F., & Gabbiani, G. (1993). Transforming Growth-Factor-Beta-1 Induces Alpha-Smooth Muscle Actin Expression in Granulation-Tissue Myofibroblasts and in Quiescent and Growing Cultured Fibroblasts. *Journal of Cell Biology*, *122*(1), 103-111. https://doi.org/10.1083/jcb.122.1.103

Dong, Z., Zhang, G. X., Qu, M., Gimple, R. C., Wu, Q. L., Qiu, Z. X.,... Rich, J. N. (2019). Targeting Glioblastoma Stem Cells through Disruption of the Circadian Clock. *Cancer Discovery*, *9*(11), 1556-1573. https://doi.org/10.1158/2159-8290.Cd-19-0215

Emlet, D. R., Gupta, P., Holgado-Madruga, M., Del Vecchio, C. A., Mitra, S. S., Han, S. Y.,... Wong, A. J. (2014). Targeting a Glioblastoma Cancer Stem-Cell Population Defined by EGF Receptor Variant III. *Cancer Res*, *74*(4), 1238-1249. https://doi.org/10.1158/0008-5472.Can-13-1407

Fan, X., Khaki, L., Zhu, T. S., Soules, M. E., Talsma, C. E., Gul, N.,... Eberhart, C. G. (2010). NOTCH Pathway Blockade Depletes CD133-Positive Glioblastoma Cells and Inhibits Growth of Tumor Neurospheres and Xenografts. *Stem Cells*, *28*(1), 5-16. https://doi.org/10.1002/stem.254

Frank, N. Y., Schatton, T., Kim, S., Zhan, Q. A., Wilson, B. J., Ma, J.,... Frank, M. H. (2011). VEGFR-1 Expressed by Malignant Melanoma-Initiating Cells Is Required for Tumor Growth. *Cancer Res*, *71*(4), 1474-1485. https://doi.org/10.1158/0008-5472.Can-10-1660

Furukawa, H., Kato, Y., Inoue, Y., Kato, T., Tada, Y., & Hashimoto, S. (2012). Correlation of Power Consumption for Several Kinds of Mixing Impellers.

International Journal of Chemical Engineering, *2012*, 1-6. https://doi.org/10.1155/2012/106496

He, H., Niu, C. S., & Li, M. W. (2012). Correlation between glioblastoma stem-like cells and tumor vascularization. *Oncology Reports*, *27*(1), 45-50. https://doi.org/10.3892/or.2011.1484

Hellstrom, M., Phng, L. K., Hofmann, J. J., Wallgard, E., Coultas, L., Lindblom, P.,... Betsholtz, C. (2007). Dll4 signalling through Notch1 regulates formation of tip cells during angiogenesis. *Nature*, *445*(7129), 776-780. https://doi.org/10.1038/nature05571

Hilbe, W., Dirnhofer, S., Oberwasserlechner, F., Schmid, T., Gunsilius, E., Hilbe, G.,... Kahler, C. M. (2004). CD133 positive endothelial progenitor cells contribute to the tumour vasculature in non-small cell lung cancer. *Journal of Clinical Pathology*, *57*(9), 965-969. https://doi.org/10.1136/jcp.2004.016444

Hristov, M., Erl, W., & Weber, P. C. (2003). Endothelial progenitor cells - Mobilization, differentiation, and homing. *Arteriosclerosis Thrombosis and Vascular Biology*, *23*(7), 1185-1189. https://doi.org/10.1161/01.Atv.0000073832.49290.B5

Hu, B., Wu, Z., & Phan, S. H. (2003). Smad3 mediates transforming growth factor-beta-induced alpha-smooth muscle actin expression. *American Journal of Respiratory Cell and Molecular Biology*, *29*(3), 397-404. https://doi.org/10.1165/rcmb.2003-0063OC

Hubert, C. G., Rivera, M., Spangler, L. C., Wu, Q. L., Mack, S. C., Prager, B. C.,... Rich, J. N. (2016). A Three-Dimensional Organoid Culture System Derived from Human Glioblastomas Recapitulates the Hypoxic Gradients and Cancer Stem Cell Heterogeneity of Tumors Found In Vivo. *Cancer Res*, *76*(8), 2465-2477. https://doi.org/10.1158/0008-5472.Can-15-2402

Ismadi, M. Z., Gupta, P., Fouras, A., Verma, P., Jadhav, S., Bellare, J., & Hourigan, K. (2014). Flow Characterization of a Spinner Flask for Induced Pluripotent Stem Cell Culture Application. *PLoS One*, *9*(10). https://doi.org/10.1371/journal.pone.0106493

Jacob, F., Salinas, R. D., Zhang, D. Y., Nguyen, P. T. T., Schnoll, J. G., Wong, S. Z. H.,... Song, H. J. (2020). A Patient-Derived Glioblastoma Organoid Model and Biobank Recapitulates Inter- and Intra-tumoral Heterogeneity. *Cell*, *180*(1), 188-+. https://doi.org/10.1016/j.cell.2019.11.036

Kaihara, T., Kawamata, H., Imura, J., Fujii, S., Kitajima, K., Omotehara, F.,... Fujimori, T. (2003). Redifferentiation and ZO-1 reexpression in liver-metastasized colorectal cancer: Possible association with epidermal growth factor receptor-induced tyrosine phosphorylation of ZO-1. *Cancer Science*, *94*(2), 166-172. https://doi.org/10.1111/j.1349-7006.2003.tb01414.x

Klein, E., Hau, A.-C., Oudin, A., Golebiewska, A., & Niclou, S. P. (2020). Glioblastoma Organoids: Pre-Clinical Applications and Challenges in the Context of Immunotherapy. *Front Oncol*, *10*. https://doi.org/10.3389/fonc.2020.604121

Lancaster, M. A., Renner, M., Martin, C. A., Wenzel, D., Bicknell, L. S., Hurles, M. E.,... Knoblich, J. A. (2013). Cerebral organoids model human brain development and microcephaly. *Nature*, *501*(7467), 373-+. https://doi.org/10.1038/nature12517

Lathia, J. D., Mack, S. C., Mulkearns-Hubert, E. E., Valentim, C. L. L., & Rich, J. N. (2015). Cancer stem cells in glioblastoma. *Genes & Development*, *29*(12), 1203-1217. https://doi.org/10.1101/gad.261982.115

Lee, G., Auffinger, B., Guo, D. N., Hasan, T., Deheeger, M., Tobias, A. L.,... Ahmed, A. U. (2016). Dedifferentiation of Glioma Cells to Glioma Stem-like Cells By Therapeutic Stress-induced HIF Signaling in the Recurrent GBM Model. *Molecular Cancer Therapeutics*, *15*(12), 3064-3076. https://doi.org/10.1158/1535-7163.Mct-15-0675

Lee, J., Kotliarova, S., Kotliarov, Y., Li, A. G., Su, Q., Donin, N. M.,... Fine, H. A. (2006). Tumor stem cells derived from glioblastomas cultured in bFGF and EGF more closely mirror the phenotype and genotype of primary tumors than do serum-cultured cell lines. *Cancer Cell*, *9*(5), 391-403. https://doi.org/10.1016/j.ccr.2006.03.030

Li, J. L., Sainson, R. C. A., Oon, C. E., Turley, H., Leek, R., Sheldon, H.,... Harris, A. L. (2011). DLL4-Notch Signaling Mediates Tumor Resistance to Anti-VEGF Therapy In Vivo. *Cancer Res*, *71*(18), 6073-6083. https://doi.org/10.1158/0008-5472.Can-11-1704

Lino, M. M., Merlo, A., & Boulay, J. L. (2010). Notch signaling in glioblastoma: a developmental drug target? *Bmc Medicine*, *8*. https://doi.org/10.1186/1741-7015-8-72

Liu, N., Zang, R., Yang, S.-T., & Li, Y. (2014). Stem cell engineering in bioreactors for large-scale bioprocessing. *Engineering in Life Sciences*, *14*(1), 4-15. https://doi.org/10.1002/elsc.201300013

Liu, S., Wang, Y. Y., Xu, K. B., Wang, Z., Fan, X., Zhang, C. B.,... Jiang, T. (2017). Relationship between necrotic patterns in glioblastoma and patient survival: fractal dimension and lacunarity analyses using magnetic resonance imaging. *Scientific Reports*, *7*. https://doi.org/10.1038/s41598-017-08862-6

Luo, P. L., Wang, Y. J., Yang, Y. Y., & Yang, J. J. (2018). Hypoxia-induced hyperpermeability of rat glomerular endothelial cells involves HIF-2 alpha mediated changes in the expression of occludin and ZO-1. *Brazilian Journal of Medical and Biological Research*, *51*(7). https://doi.org/10.1590/1414-431X20186201

Matter, K., Aijaz, S., Tsapara, A., & Balda, M. S. (2005). Mammalian tight junctions in the regulation of epithelial differentiation and proliferation. *Current Opinion in Cell Biology*, *17*(5), 453-458. https://doi.org/10.1016/j.ceb.2005.08.003

Nakano, I., Garnier, D., Minata, M., & Rak, J. (2015). Extracellular vesicles in the biology of brain tumour stem cells--Implications for inter-cellular communication, therapy and biomarker development. *Semin Cell Dev Biol*, *40*, 17-26. https://doi.org/10.1016/j.semcdb.2015.02.011

Ogawa, J., Pao, G. M., Shokhirev, M. N., & Verma, I. M. (2018). Glioblastoma Model Using Human Cerebral Organoids. *Cell Reports*, *23*(4), 1220-1229. https://doi.org/10.1016/j.celrep.2018.03.105

Ostrom, Q. T., Patil, N., Cioffi, G., Waite, K., Kruchko, C., & Barnholtz-Sloan, J. S. (2020). CBTRUS Statistical Report: Primary Brain and Other Central Nervous System Tumors Diagnosed in the United States in 2013-2017. *Neuro Oncol*, *22*, 1-42. https://doi.org/10.1093/neuonc/noaa200

Panchalingam, K. M., Paramchuk, W. J., Chiang, C. Y., Shah, N., Madan, A., Hood, L.,... Behie, L. A. (2010). Bioprocessing of human glioblastoma brain cancer tissue. *Tissue Eng Part A*, *16*(4), 1169-1177. https://doi.org/10.1089/ten.tea.2009.0490

Park, K. S., Kang, S. N., Kim, D. H., Kim, H. B., Im, K. S., Park, W.,... Joung, Y. K. (2020). Late endothelial progenitor cell-capture stents with CD146 antibody and nanostructure reduce in-stent restenosis and thrombosis. *Acta Biomaterialia*, *111*, 91-101. https://doi.org/10.1016/j.actbio.2020.05.011

Patrizii, M., Bartucci, M., Pine, S. R., & Sabaawy, H. E. (2018). Utility of Glioblastoma Patient-Derived Orthotopic Xenografts in Drug Discovery and Personalized therapy. *Front Oncol*, *8*. https://doi.org/10.3389/fonc.2018.00023

Ricci-Vitiani, L., Pallini, R., Biffoni, M., Todaro, M., Invernici, G., Cenci, T.,... De Maria, R. (2011). Tumour vascularization via endothelial differentiation of glioblastoma stem-like cells (vol 468, pg 824, 2010). *Nature*, *477*(7363), 238-238. https://doi.org/10.1038/nature10410

Rocha, R., Torres, A., Ojeda, K., Uribe, D., Rocha, D., Erices, J.,... Quezada, C. (2018). The Adenosine A(3) Receptor Regulates Differentiation of Glioblastoma Stem-Like Cells to Endothelial Cells under Hypoxia. *International Journal of Molecular Sciences*, *19*(4). https://doi.org/10.3390/ijms19041228

Rong, Y., Durden, D. L., Van Meir, E. G., & Brat, D. J. (2006). 'Pseudopalisading' necrosis in glioblastoma: A familiar morphologic feature that links vascular pathology, hypoxia, and angiogenesis. *J Neuropathol Exp Neurol*, *65*(6), 529-539. https://doi.org/10.1097/00005072-200606000-00001

Shah, S. S., Rodriguez, G. A., Musick, A., Walters, W. M., De Cordoba, N., Barbarite, E.,... Graham, R. M. (2019). Targeting Glioblastoma Stem Cells with 2-Deoxy-D-Glucose (2-DG) Potentiates Radiation-Induced Unfolded Protein Response (UPR). *Cancers*, *11*(2). https://doi.org/10.3390/cancers11020159

Sherry, M. M., Reeves, A., Wu, J. L. K., & Cochran, B. H. (2009). STAT3 Is Required for Proliferation and Maintenance of Multipotency in Glioblastoma Stem Cells. *Stem Cells*, *27*(10), 2383-2392. https://doi.org/10.1002/stem.185

Stockhausen, M. T., Kristoffersen, K., & Poulsen, H. S. (2010). The functional role of Notch signaling in human gliomas. *Neuro Oncol*, *12*(2), 199-211. https://doi.org/10.1093/neuonc/nop022

Suva, M. L., Rheinbay, E., Gillespie, S. M., Patel, A. P., Wakimoto, H., Rabkin, S. D.,... Bernstein, B. E. (2014). Reconstructing and Reprogramming the Tumor-Propagating Potential of Glioblastoma Stem-like Cells. *Cell*, *157*(3), 580-594. https://doi.org/10.1016/j.cell.2014.02.030

Tilson, S. G., Haley, E. M., Triantafillu, U. L., Dozier, D. A., Langford, C. P., Gillespie, G. Y., & Kim, Y. (2015). ROCK Inhibition Facilitates In Vitro Expansion of Glioblastoma Stem-Like Cells. *PLoS One*, *10*(7), e0132823. https://doi.org/10.1371/journal.pone.0132823

Timmermans, F., Plum, J., Yoder, M. C., Ingram, D. A., Vandekerckhove, B., & Case, J. (2009). Endothelial progenitor cells: identity defined? *Journal of Cellular and Molecular Medicine*, *13*(1), 87-102. https://doi.org/10.1111/j.1582-4934.2008.00598.x

van Linde, M. E., Brahm, C. G., Hamer, P. C. D., Reijneveld, J. C., Bruynzeel, A. M. E., Vandertop, W. P.,... Verheul, H. M. W. (2017). Treatment outcome of patients with recurrent glioblastoma multiforme: a retrospective multicenter analysis. *J Neurooncol*, *135*(1), 183-192. https://doi.org/10.1007/s11060-017-2564-z

Vora, P., Venugopal, C., Salim, S. K., Tatari, N., Bakhshinyan, D., Singh, M.,... Singh, S. (2020). The Rational Development of CD133-Targeting Immunotherapies for

Glioblastoma. *Cell Stem Cell*, *26*(6), 832-+. https://doi.org/10.1016/j.stem.2020.04.008

Wang, X. X., Prager, B. C., Wu, Q. L., Kim, L. J. Y., Gimple, R. C., Shi, Y.,... Rich, J. N. (2018). Reciprocal Signaling between Glioblastoma Stem Cells and Differentiated Tumor Cells Promotes Malignant Progression. *Cell Stem Cell*, *22*(4), 514-+. https://doi.org/10.1016/j.stem.2018.03.011

Warshamana, G. S., Corti, M., & Brody, A. R. (2001). TNF-alpha, PDGF, and TGF-beta(1) expression by primary mouse bronchiolar-alveolar epithelial and mesenchymal cells: TNF-alpha induces TGF-beta(1). *Experimental and Molecular Pathology*, *71*(1), 13-33. https://doi.org/10.1006/exmp.2001.2376

Xing, T. S., Benderman, L. L. A. M. N., Sabu, T. Y., Parker, O. E., Yang, E. R., Lu, Q.,... Chen, Y. H. (2020). Tight Junction Protein Claudin-7 Is Essential for Intestinal Epithelial Stem Cell Self-Renewal and Differentiation. *Cellular and Molecular Gastroenterology and Hepatology*, *9*(4), 641-659. https://doi.org/10.1016/j.jcmgh.2019.12.005

Xiu, M. X., Liu, Y. M., & Kuang, B. H. (2020). The oncogenic role of Jagged1/Notch signaling in cancer. *Biomedicine & Pharmacotherapy*, *129*. https://doi.org/10.1016/j.biopha.2020.110416

Xu, J. L., Lim, S. B. H., Ng, M. Y., Ali, S. M., Kausalya, J. P., Limviphuvadh, V.,... Hunziker, W. (2012). ZO-1 Regulates Erk, Smad1/5/8, Smad2, and RhoA Activities to Modulate Self-Renewal and Differentiation of Mouse Embryonic Stem Cells. *Stem Cells*, *30*(9), 1885-1900. https://doi.org/10.1002/stem.1172

Yoshimatsu, Y., Wakabayashi, I., Kimuro, S., Takahashi, N., Takahashi, K., Kobayashi, M.,... Watabe, T. (2020). TNF-α enhances TGF-β-induced endothelial-to-mesenchymal transition via TGF-β signal augmentation. *Cancer Science*, *111*(7), 2385-2399. https://doi.org/10.1111/cas.14455

Zhu, T. S., Costello, M. A., Talsma, C. E., Flack, C. G., Crowley, J. G., Hamm, L. L.,... Fan, X. (2011). Endothelial Cells Create a Stem Cell Niche in Glioblastoma by Providing NOTCH Ligands That Nurture Self-Renewal of Cancer Stem-Like Cells. *Cancer Res*, *71*(18), 6061-6072. https://doi.org/10.1158/0008-5472.Can-10-4269

Zhu, V. F., Yang, J. X., LeBrun, D. G., & Li, M. (2012). Understanding the role of cytokines in Glioblastoma Multiforme pathogenesis. *Cancer Lett*, *316*(2), 139-150. https://doi.org/10.1016/j.canlet.2011.11.001

Figure Captions

Figure 1

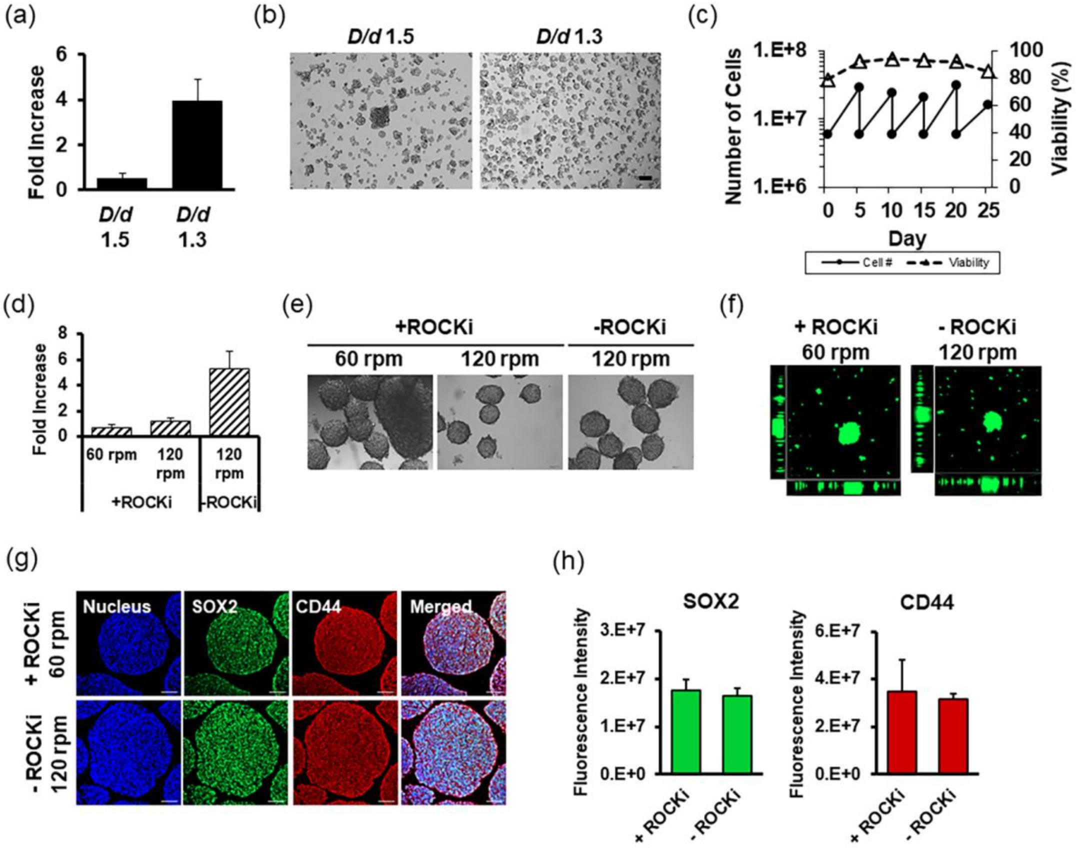

Figure 1. Optimization of glioblastoma organoid (GBO) production. (a) Cell number increase (represented as fold change compared to initial cell seeding) after 5 days of culture in two different bioreactors (BR1: *D/d* 1.5; BR2: *D/d* 1.3) at 60 rpm. $p < 0.05$, n ≥ 3. (b) Brightfield images of GBO. Scale bar: 100 μm. (c) Continuous U87 culture in the BR2 configuration. Cells were passaged every 5 days (represented by vertical lines) with the same inoculation density. (d) Inhibition of cell proliferation by Y-27632 Rho-associated protein kinase inhibitor (ROCKi). Cell number increase (represented as fold change compared to initial cell seeding) after 5 days of culture in the BR2 configuration with 60 and 120 rpm agitation. (e) Brightfield images of GBOs in BR2 with 60 and 120 rpm and with and without ROCKi. Scale bar: 100 μm. (f) Perspective views of live and dead cells in GBO. Main square: top view; left panel: side view; and bottom

panel:front view. Green: live cells, red: apoptotic cells. (g) Immunohistochemistry (IHC) of GBO stained for SOX2 in green and CD44 in red. Nucleus in blue. Scale bar: 100 µm. (h) Quantified fluorescence intensity of SOX2 and CD44 by CTCF; n>10; mean ± SD.

Figure 2

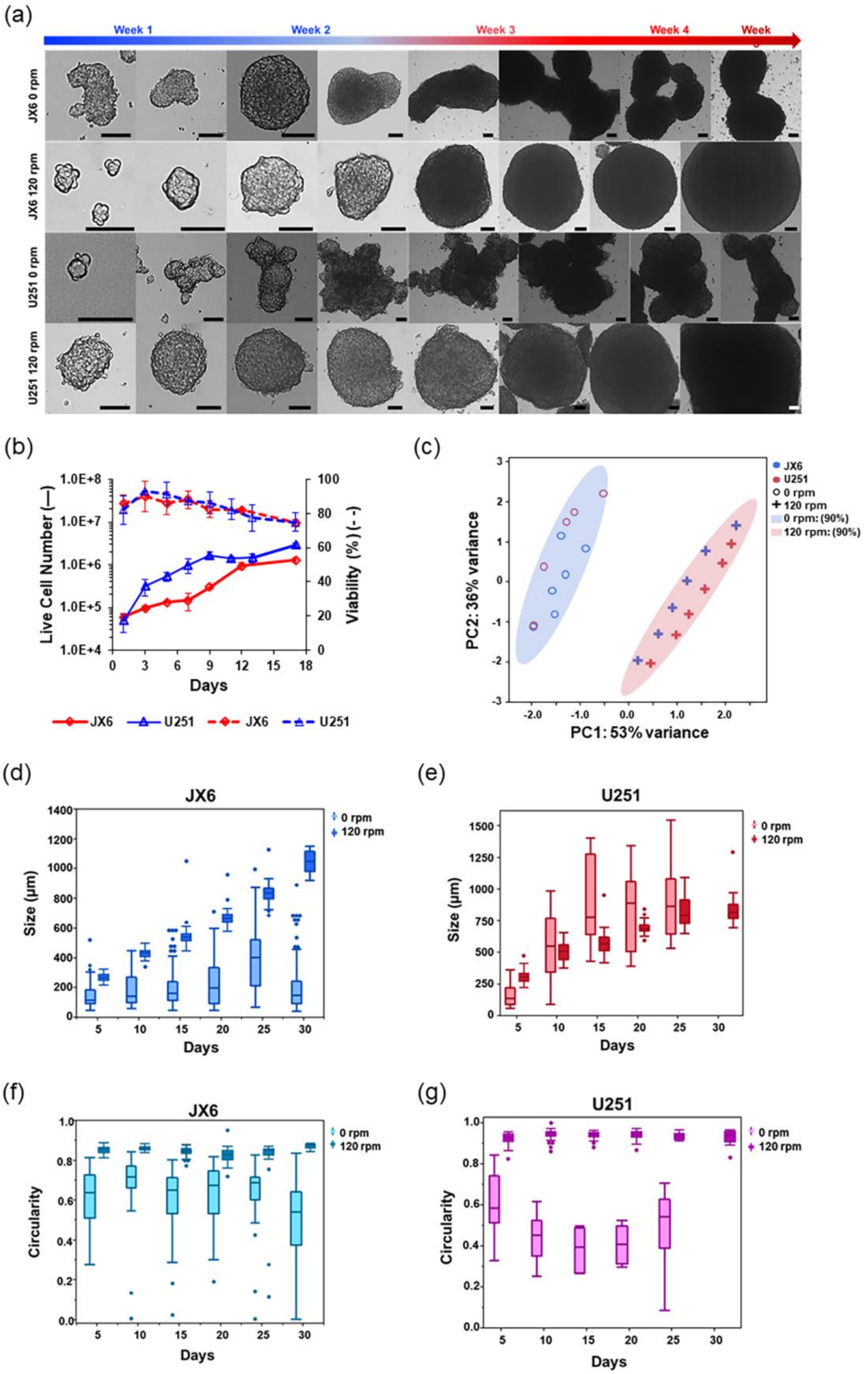
(a)
Week 1
Week 2
Week 3
Week 4
Week
JX6 0 rpm
JX6 120 rpm
U251 0 rpm
U251 120 rpm
(b)
Live Cell Number (—)
Viability (%) (- -)
1.0E+8
1.0E+7
1.0E+6
1.0E+5
1.0E+4
100
80
60
40
20
0
0
3
6
9
12
15
18
Days
JX6
U251
JX6
U251
(c)
PC2: 36% variance
PC1: 53% variance
3
2
1
0
-1
-2
-3
-2.0
-1.0
0.0
1.0
2.0
JX6
U251
0 rpm
120 rpm
0 rpm: (90%)
120 rpm: (90%)
(d)
JX6
Size (µm)
1400
1200
1000
800
600
400
200
0
5
10
15
20
25
30
Days
0 rpm
120 rpm
(e)
U251
Size (µm)
1500
1250
1000
750
500
250
0
5
10
15
20
25
30
Days
0 rpm
120 rpm
(f)
JX6
Circularity
1.0
0.8
0.6
0.4
0.2
0.0
5
10
15
20
25
30
Days
0 rpm
120 rpm
(g)
U251
Circularity
1.0
0.8
0.6
0.4
0.2
0.0
5
10
15
20
25
30
Days
0 rpm
120 rpm

Figure 2. Production of large GBOs within 5 weeks. (a) U251 and JX6 GBOs generated from the bioreactors (120 rpm; bGBO) and tissue culture polystyrene (0 rpm; tGBO). Culture period is indicated above the images by week. Scale bar: 100 µm. (b) Growth curves of JX6 (diamonds) and U251 (triangles) bGBOs. Solid line: live cell number, dotted line: cell viability. n > 3; mean ± SD. (c) Principal component analysis (PCA) plot of diameter and circularity for the JX6 (blue) and U251 (red) tGBOs (0 rpm) and bGBOs (120 rpm) with 90% confidence ellipses (light blue: 0 rpm, light red: 120 rpm). ○: 0 rpm and +: 120 rpm. (d) and (e) Box and whisker plot of the size distribution of JX6 (d) and U251 (e) tGBOs (0 rpm) and bGBOs (120 rpm). (f) and (g) Box and whisker plot of the circularity of JX6 (f) and U251 (g) tGBOs (0 rpm) and bGBOs (120 rpm).

Figure 3

(a)

tGBO (0 rpm)

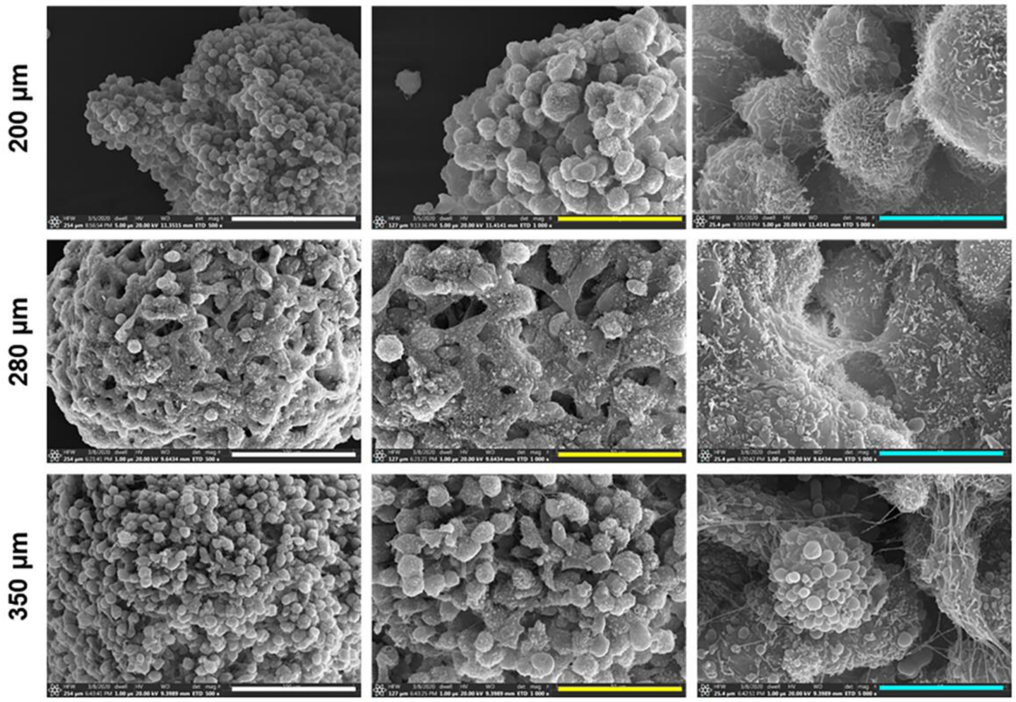

(b)

bGBO (120 rpm)

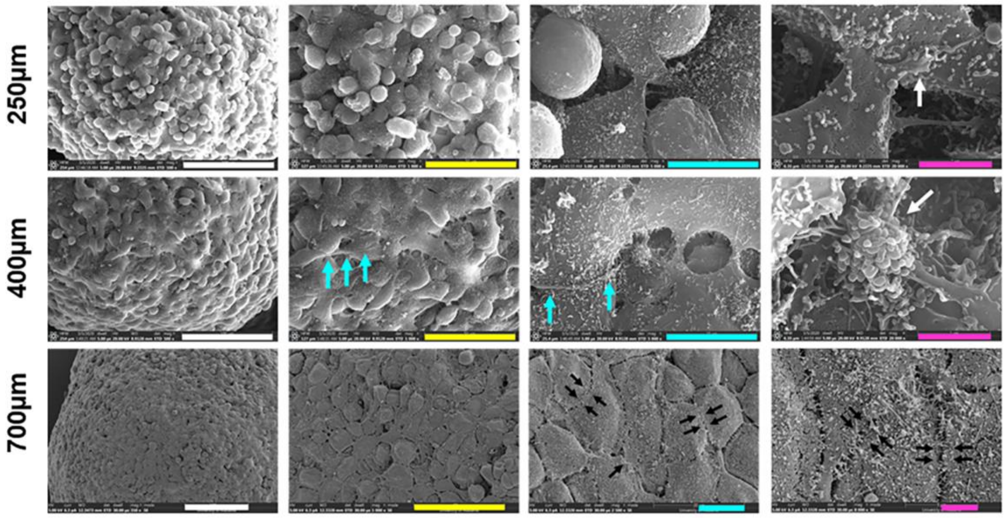

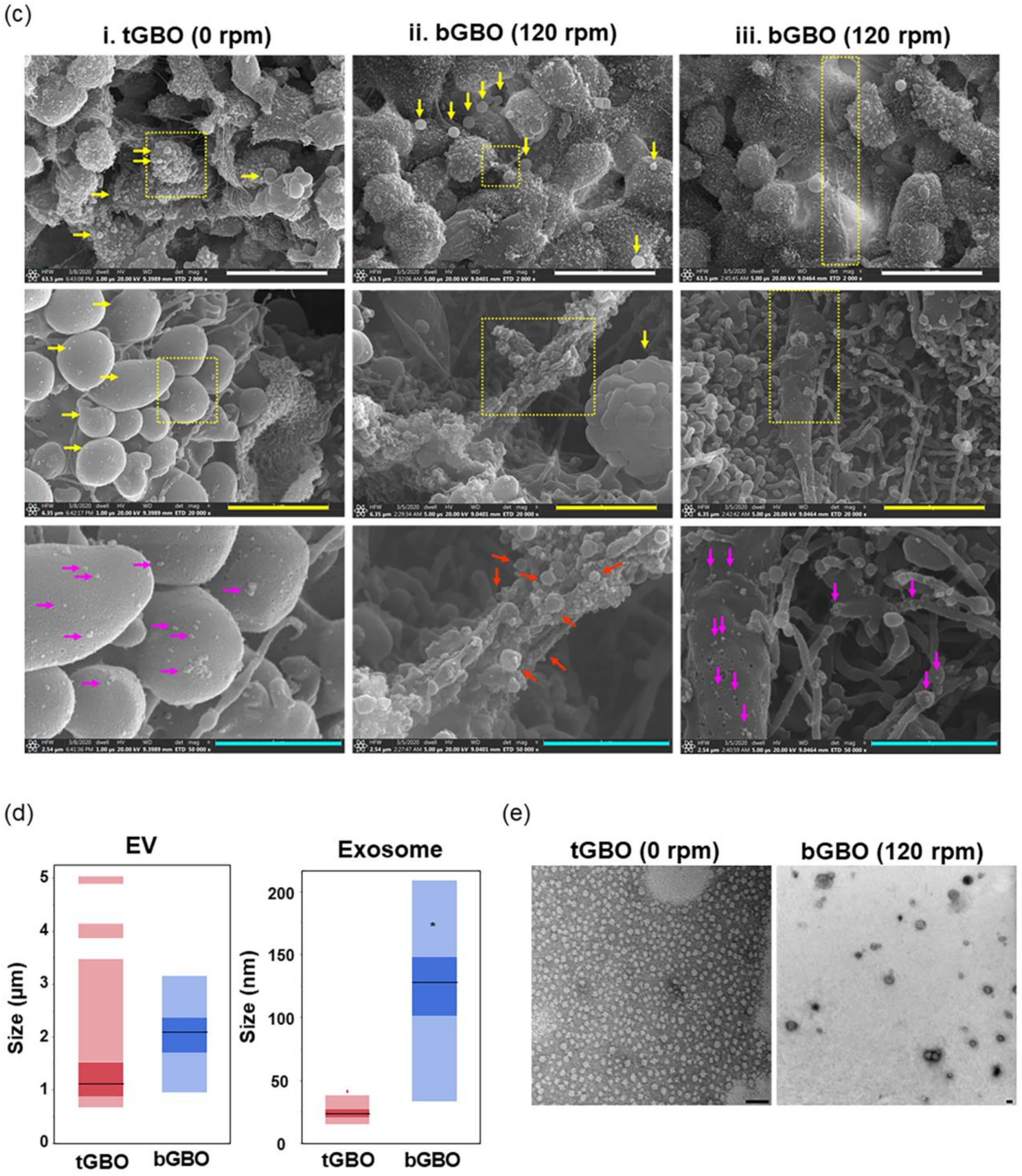

Figure 3. SEM and TEM image analyses of tGBOs and bGBOs and their extracellular (EVs). (a) SEM images of tGBOs (0 rpm) and (b) bGBOs (120 rpm). Cyan arrows: axon-like long protrusion. White arrows: strong cell-to-cell interactions. Black arrows: tight junctions. (a) and (b) Average diameters of GBOs are indicated on the left side. Scale bars: white 100 µm, yellow 50 µm, cyan 10 µm, and pink 2 µm. (c) SEM images of EVs on the tGBO and bGBO. (i) tGBO,

(ii) bGBO, and (iii) bGBO with an axon-like long protrusion. Yellow boxes: higher magnification images in the second and third rows; yellow arrows: budding EVs; magenta arrows: exosomes; red arrows: larger size exosomes than those in (i) and (iii). Scale bars: white 20 nm, yellow 2 nm, and cyan 1 nm. (d) High density region (HDR) plot for the size of EVs and exosomes. Dark boxes represent the 50% highest cumulative of the total population. Lighter boxes represent 99% cumulative probability of the total population. The red point represents outlier with 99% probability. The mode lines are in black. $^*p < 0.05$ (e) TEM images of exosomes secreted in the conditioned media of tGBO and bGBO cultures collected after 14 days. Scale bars: 100 nm.

Figure 4

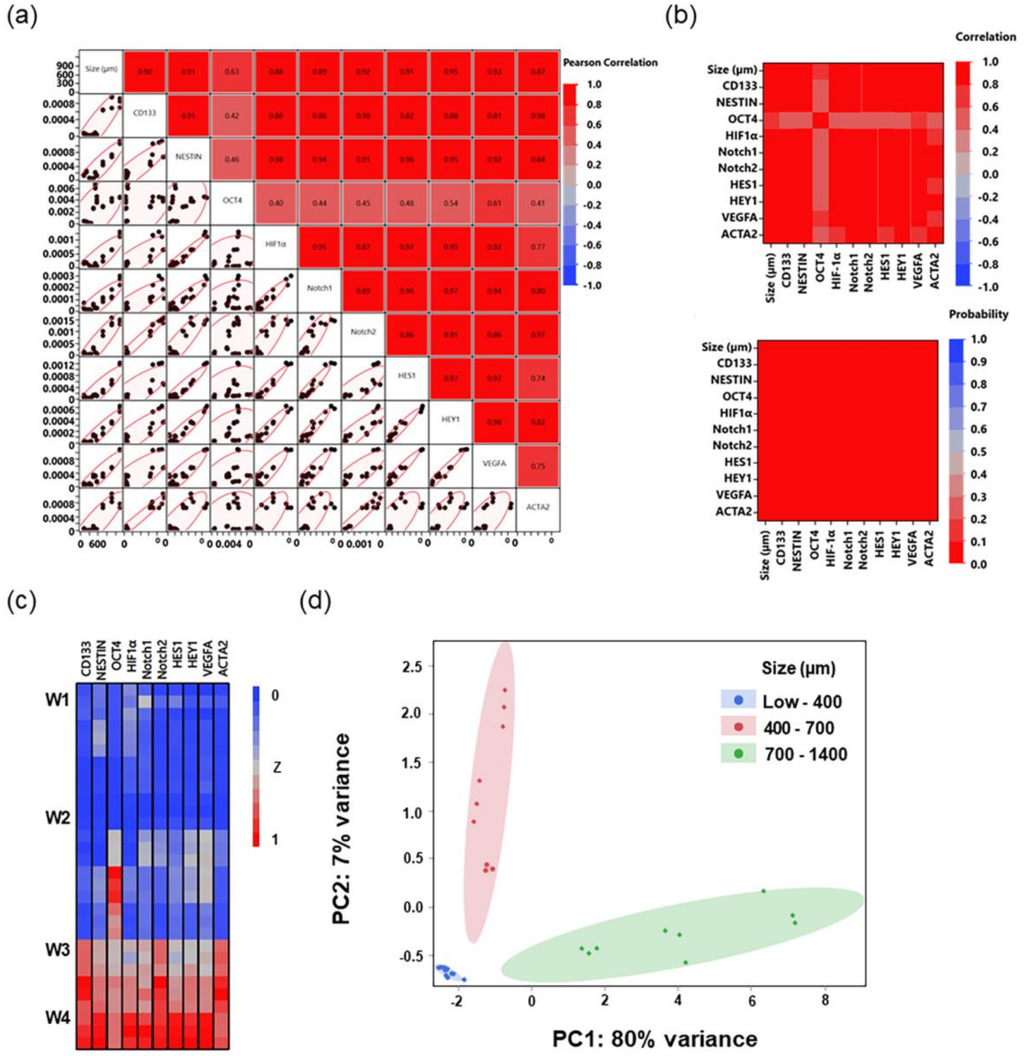
(a)
Pearson Correlation
Size (µm)
CD133
NESTIN
OCT4
HIF1α
Notch1
Notch2
HES1
HEY1
VEGFA
ACTA2
(b)
Correlation
Probability
(c)
W1
W2
W3
W4
Z
(d)
Size (µm)
Low - 400
400 - 700
700 - 1400
PC1: 80% variance
PC2: 7% variance

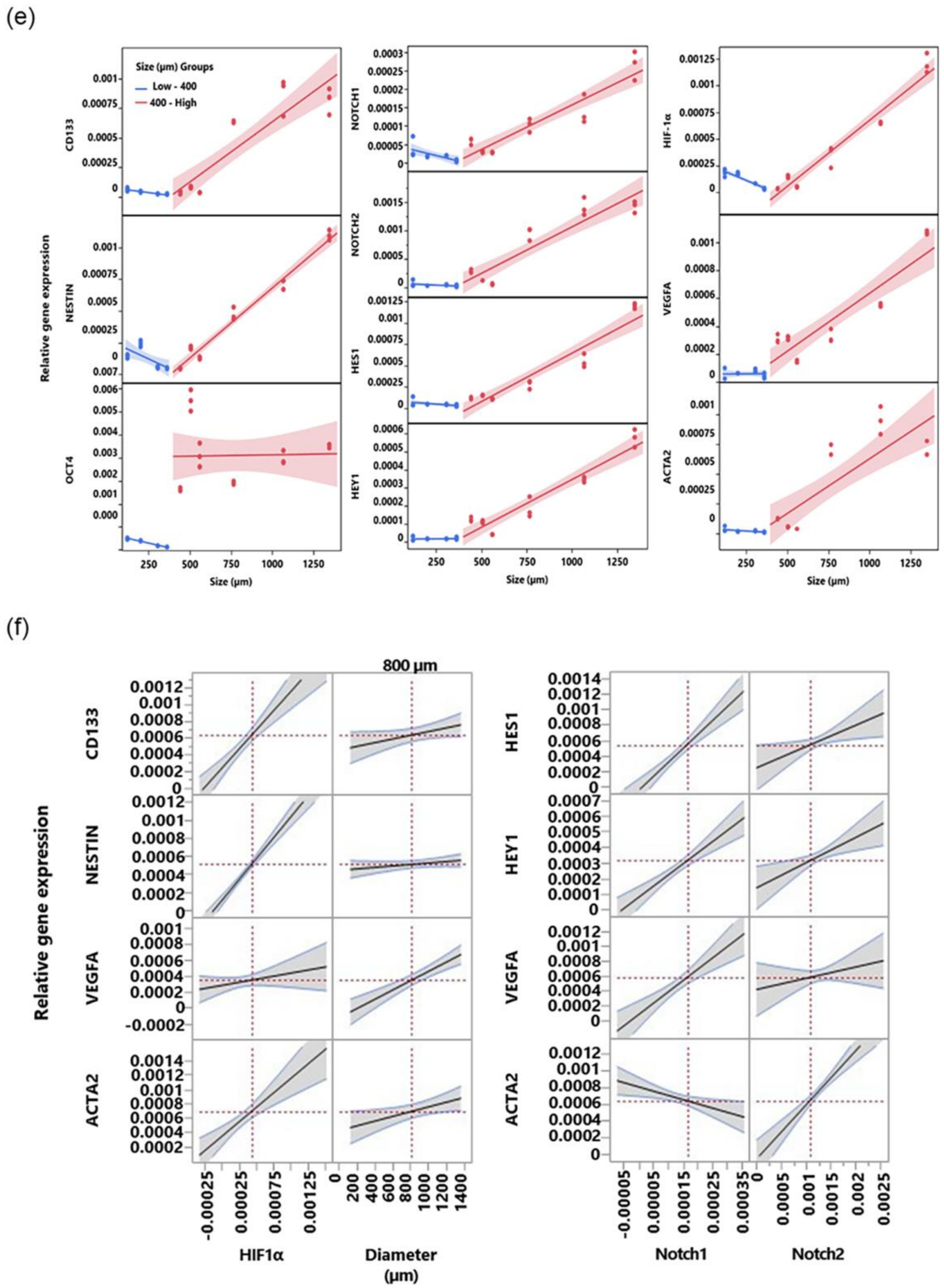

Figure 4. Multivariate analysis of gene expression in U251 bGBOs. (a) Scatter plot matrix of gene expression and the bGBO size (white boxes) and the corresponding Pearson correlation coefficients (shaded heatmap boxes). The y-axis of the top left corner box and the x-axis of the

bottom left corner box are the size (diameter) of the bGBOs in μm. Other boxes' axes indicate relative gene expression. (b) Heatmap of Pearson correlations (left) and their probability p-values (right) between the size and the molecular profiles of heterogeneous GBOs. (c) Cell plot of gene expression level by each week of culture (W) with normalized gene expression (Z) to the Day 1 gene expression. (d) Principal components analysis (PCA) plot of U251 gene expression for different sizes of the bGBOs with 90% confidence ellipses (shaded ellipses). Blue: bGBO < 400 μm; red: 400 μm < bGBO < 700 μm; green bGBO >700 μm. (e) Relative expression levels of each gene (y-axis) by the size of bGBO (x-axis). R^2 values are in the table below the graphs (f) Predictive gene expression profiles according to the size of the bGBO and relative gene expression of HIF-1α, NOTCH1, and NOTCH2. The x-axes indicate the bGBO size in μm and relative gene expression for each gene. 95% confidence interval are shown in gray. Red dotted lines indicate the predicted size and gene expression of HIF-1α, NOTCH1, and NOTCH2.

Figure 5

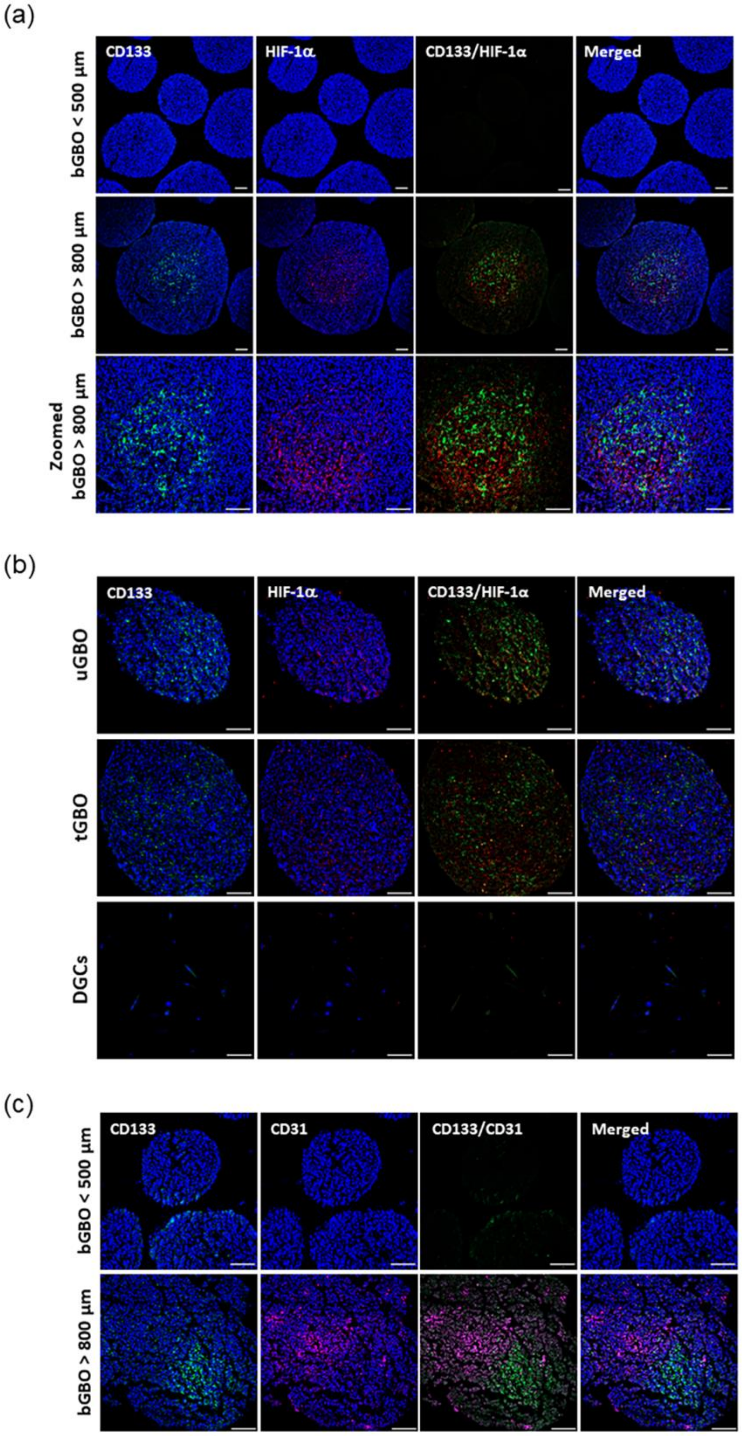
(a)
CD133
HIF-1α
CD133/HIF-1α
Merged
bGBO < 500 µm
bGBO > 800 µm
Zoomed bGBO > 800 µm
(b)
CD133
HIF-1α
CD133/HIF-1α
Merged
uGBO
tGBO
DGCs
(c)
CD133
CD31
CD133/CD31
Merged
bGBO < 500 µm
bGBO > 800 µm

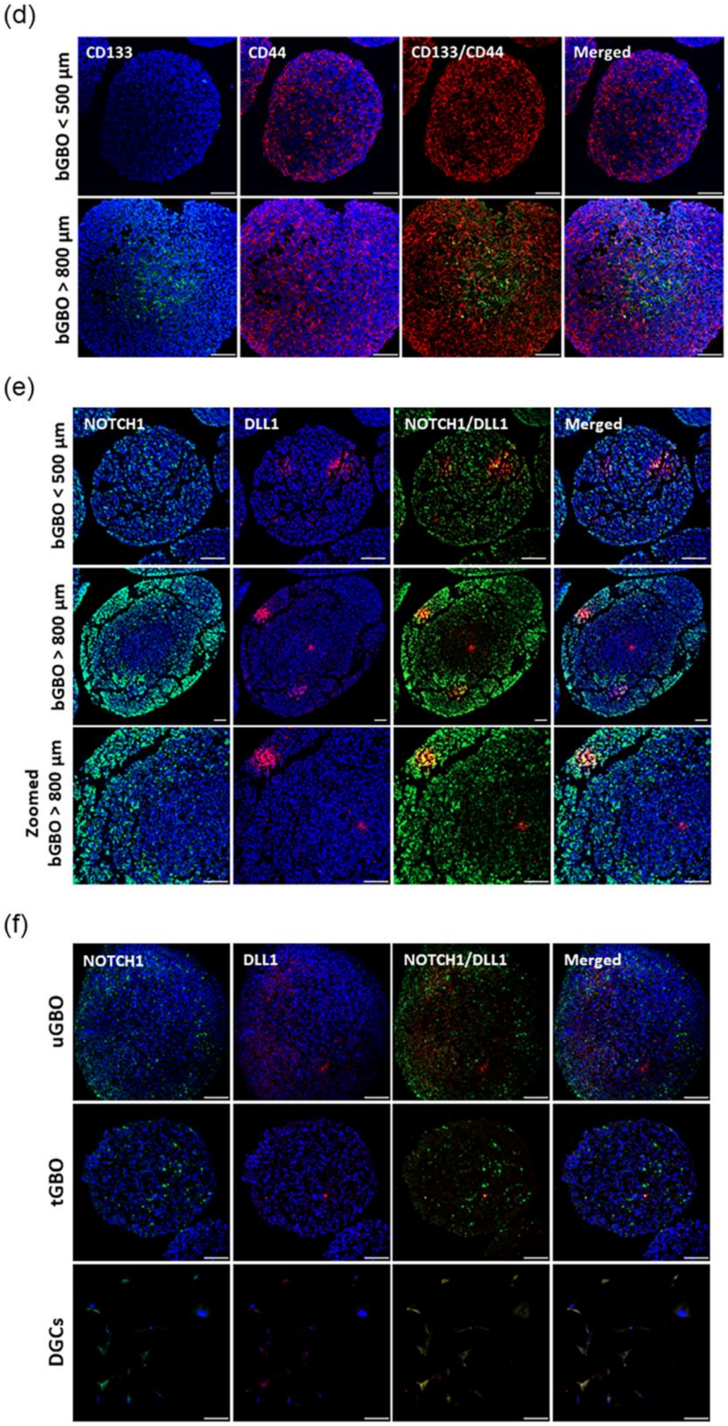
(d)
CD133
CD44
CD133/CD44
Merged
bGBO < 500 µm
bGBO > 800 µm
(e)
NOTCH1
DLL1
NOTCH1/DLL1
Merged
bGBO < 500 µm
bGBO > 800 µm
Zoomed bGBO > 800 µm
(f)
NOTCH1
DLL1
NOTCH1/DLL1
Merged
uGBO
tGBO
DGCs

(g)

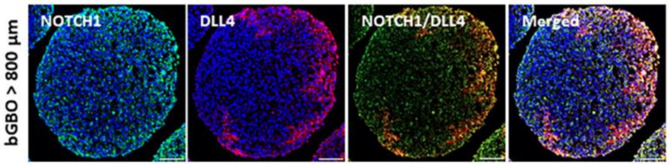
bGBO > 800 µm
NOTCH1
DLL4
NOTCH1/DLL4
Merged

(h)

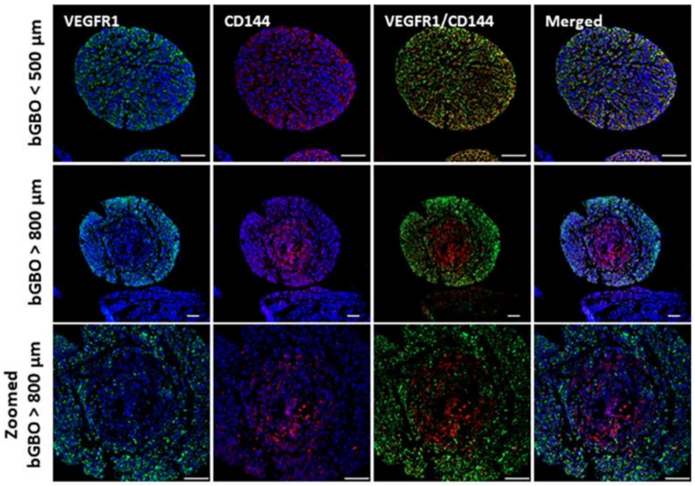
VEGFR1
CD144
VEGFR1/CD144
Merged
bGBO < 500 µm
bGBO > 800 µm
Zoomed
bGBO > 800 µm

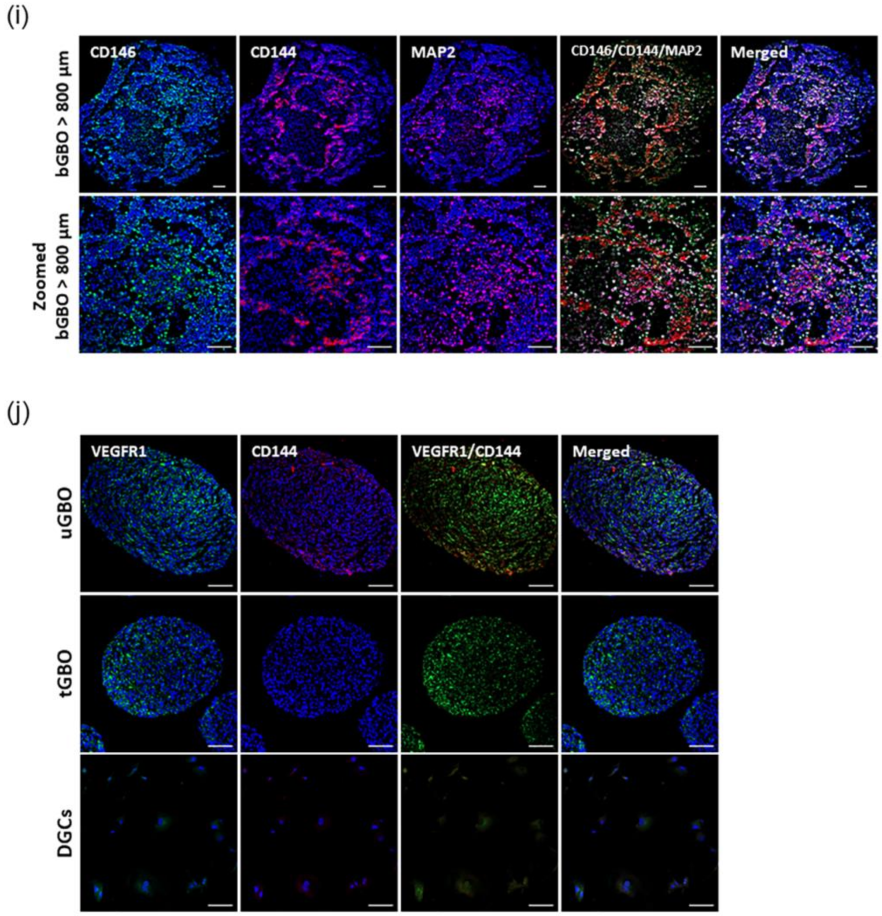

Figure 5. Size-dependent heterogeneous glioblastoma stem cell (GSC) niche model in JX6 PDX GBOs. (a), (e), (h), and (i): IHC of different sizes of JX6 bGBOs, with higher magnification of images in the bottom rows. (b), (f), and (j): IHC of uGBOs, tGBOs, and DGCs. (a) and (b) IHC of GBO stained for GSC marker: CD133 (green) and hypoxic marker: HIF-1α (red). (c) IHC of bGBOs for CD133 (green) and endothelial cell marker: CD31 (purple). (d) IHC of bGBOs stained for GSC markers: CD133 (green) and CD44 (red). (e) and (f) IHC of GBOs stained for GSC marker: NOTCH1 (green) and NOTCH ligand: DLL1 (red). (g) IHC of bGBO stained for NOTCH1 (green) and NOTCH ligand: DLL4 (red). (h) IHC of GBO stained for angiogenesis marker: VEGFR1 (green) and endothelial cell marker: CD144 (red). (i) IHC of bGBO stained for pericyte marker: CD146 (green), endothelial cell marker: CD144 (red), and astrocyte marker:

MAP2 (purple). (j) IHC of uGBO, tGBO, and DGBO stained for angiogenesis marker: VEGFR1 (green), endothelial cell marker: CD144 (red). (a)-(j) Nuclei (blue). Scale bar: 100 µm.

Figure 6

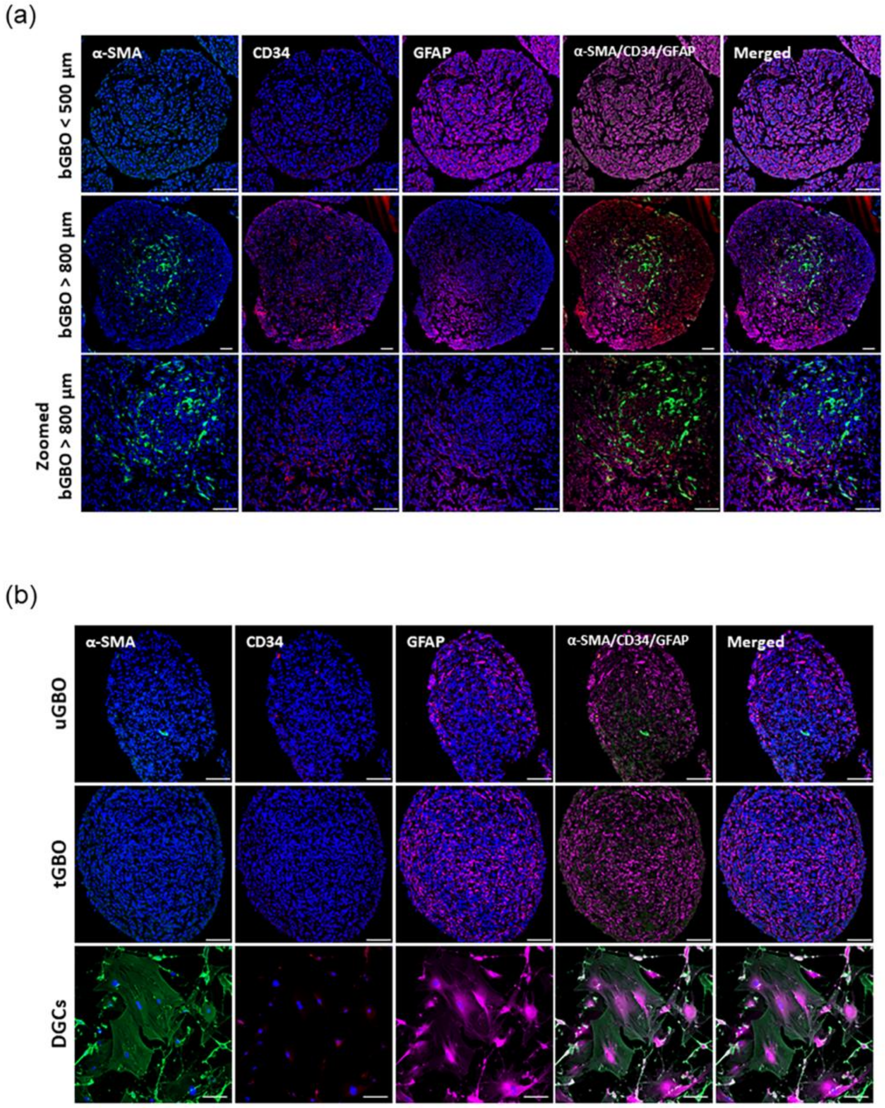

(c)

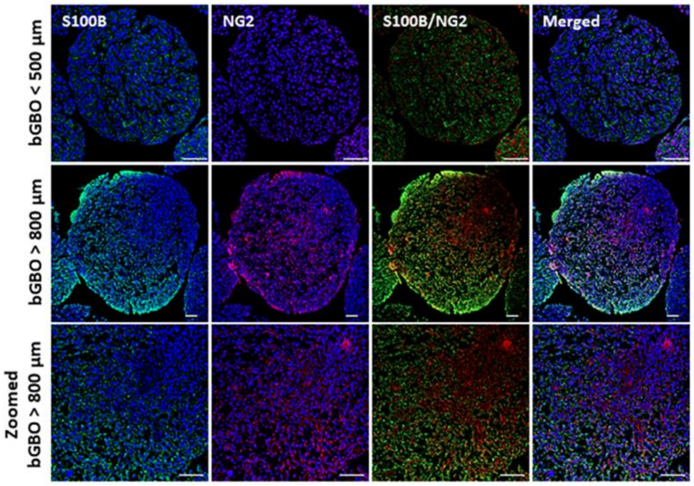
S100B
NG2
S100B/NG2
Merged
bGBO < 500 µm
bGBO > 800 µm
Zoomed
bGBO > 800 µm

(d)

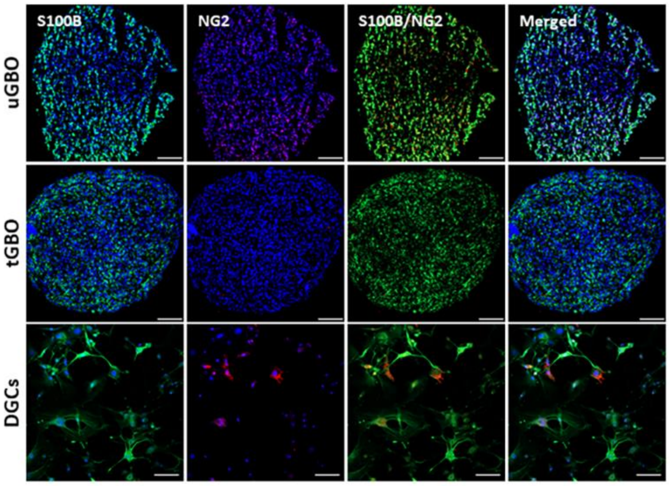
S100B
NG2
S100B/NG2
Merged
uGBO
tGBO
DGCs

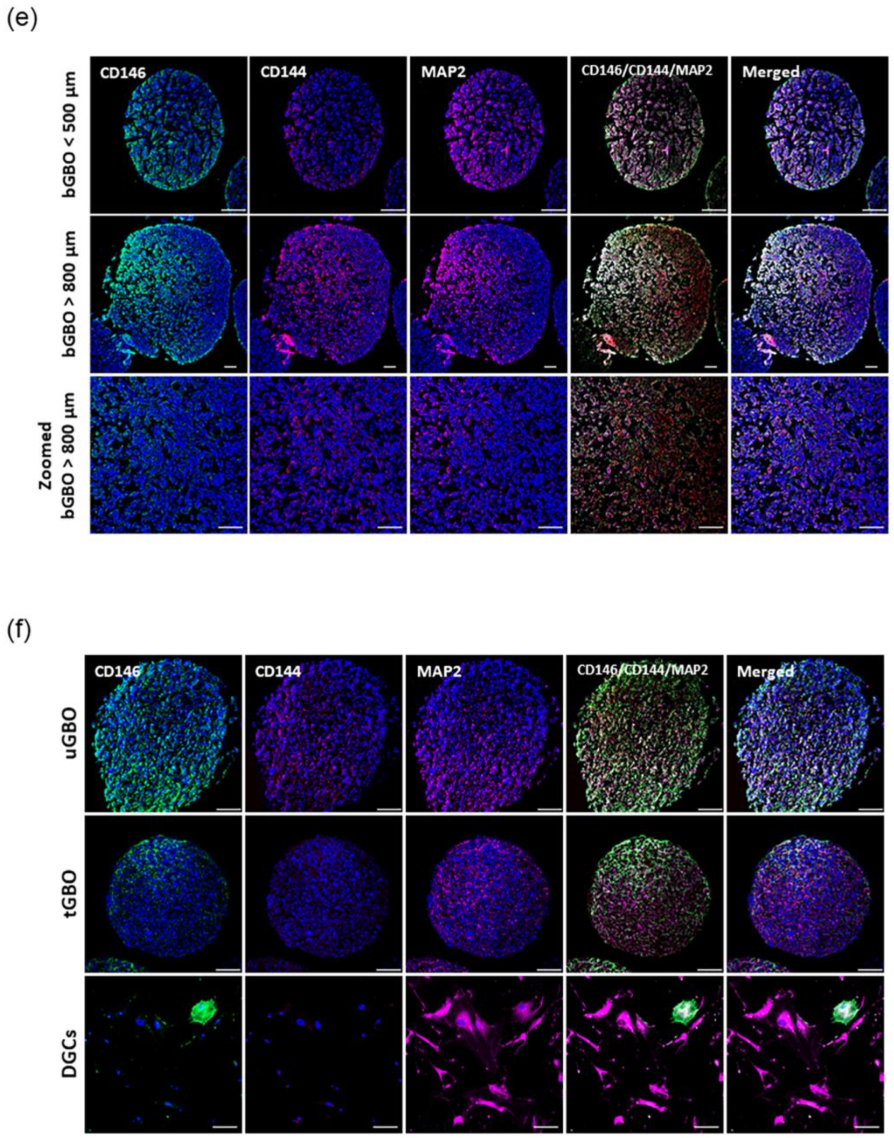

Figure 6. Transdifferentiated GBM and their spatial distribution in JX6 GBOs. (a), (c), and (e) IHC of different size of JX6 bGBOs with higher magnification images in the bottom rows. (b), (d), and (f) IHC of uGBOs, tGBOs, and JX6 DGCs. (a) and (b) Pericyte marker: α-SMA (green), endothelial cell marker: CD34 (red), and astrocyte marker: GFAP (purple). (c) and (d) astrocyte marker: S100B (green) and pericyte marker: NG2 (red). (e) and (f) Pericyte marker: CD146 (green), endothelial cell marker: CD144 (red), and astrocyte marker: MAP2 (purple). (a)-(f) Nuclei (blue). Scale bar: 100 μm.

Figure 7

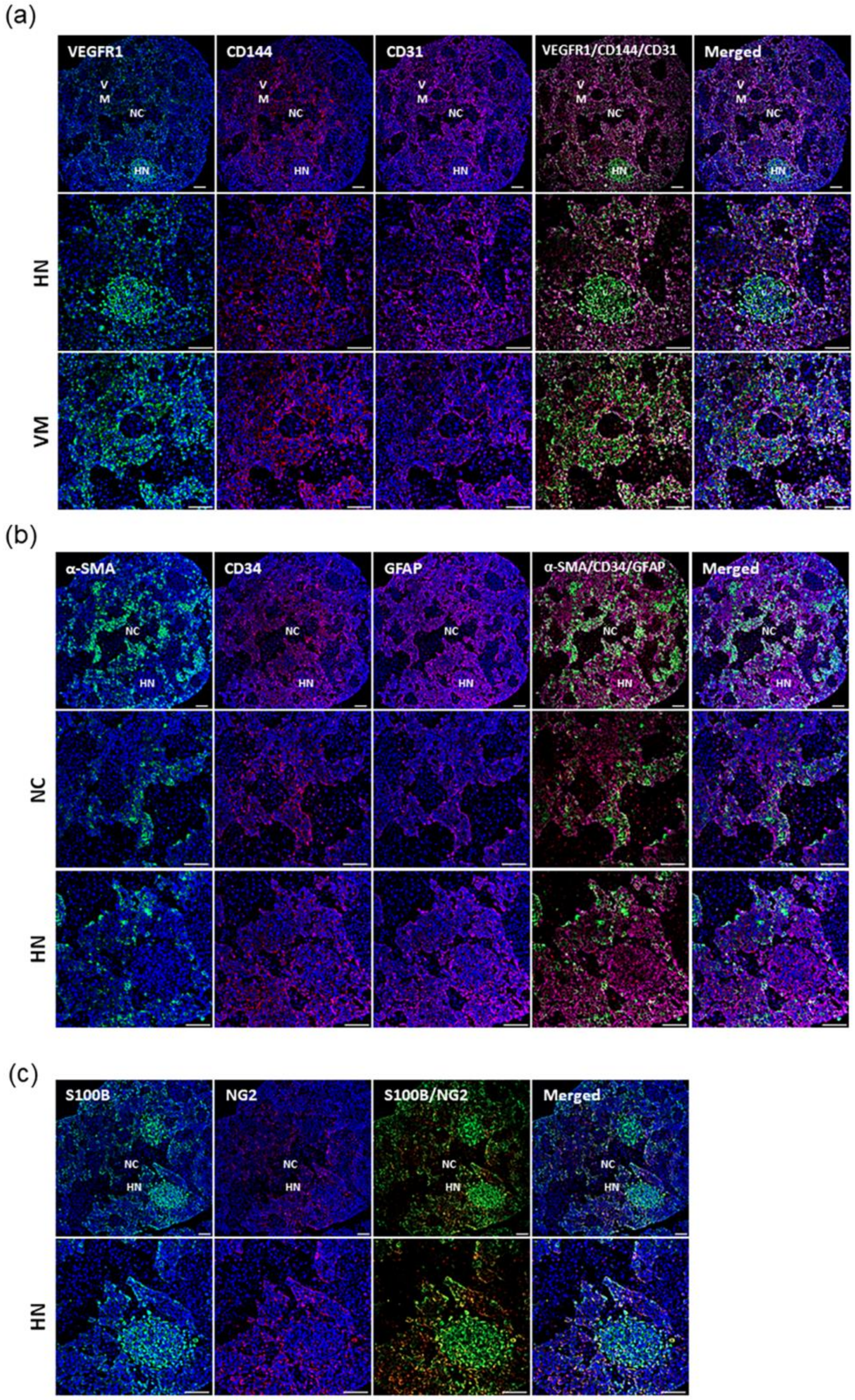
(a)
VEGFR1
CD144
CD31
VEGFR1/CD144/CD31
Merged
V
M
NC
HN
HN
VM
(b)
α-SMA
CD34
GFAP
α-SMA/CD34/GFAP
Merged
NC
HN
NC
HN
(c)
S100B
NG2
S100B/NG2
Merged
NC
HN
HN

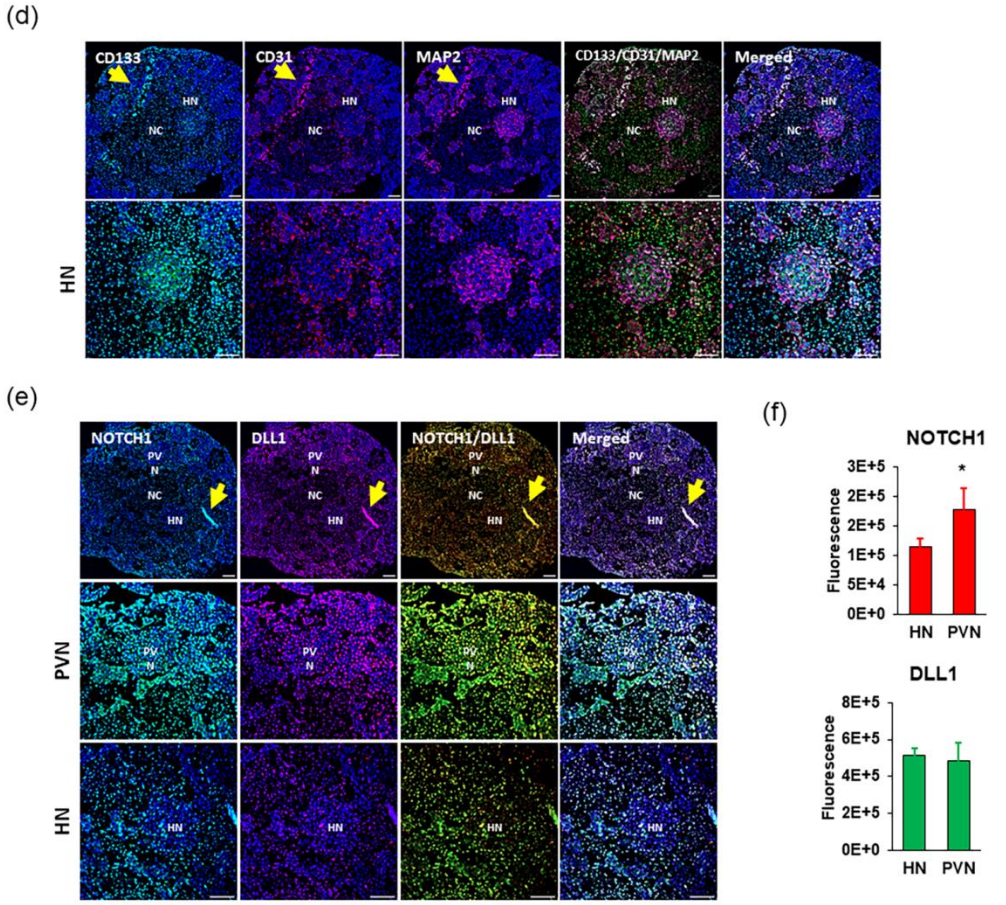

Figure 7. GBM TME containing necrotic core. (a)-(e) IHC of JX6 bGBO with higher magnification images of the indicated regions in the bottom two rows. (a) Angiogenesis marker: VEGFR1 (green), endothelial cell marker: CD144 (red), and endothelial cell marker: CD31 (purple). (b) Pericyte marker: α-SMA (green), endothelial cell marker: CD34 (red), and astrocyte marker: GFAP (purple). (c) Astrocyte marker: S100B (green) and pericyte marker: NG2 (red). (d) GSC marker: CD133 (green), endothelial cell marker: CD31 (red), and astrocyte marker: MAP2 (purple). Arrows indicate a wrinkled artifact on the sectioned bGBO. (e) GSC marker and its ligand: NOTCH1 (green) and DLL1 (red). Arrows indicate a defect during the sample preparation. (a)-(e) Nuclei (blue). NC: necrotic core, VM: vasculogenic mimicry, HN: hypoxic

niche, and PVN: perivascular niche. Scale bar: 100 µm. (f) Quantified intensity of NOTCH1 and DLL1 in HN and PVN by CTCF. *$p < 0.05$, n > 10; mean ± SD.

Figure 8

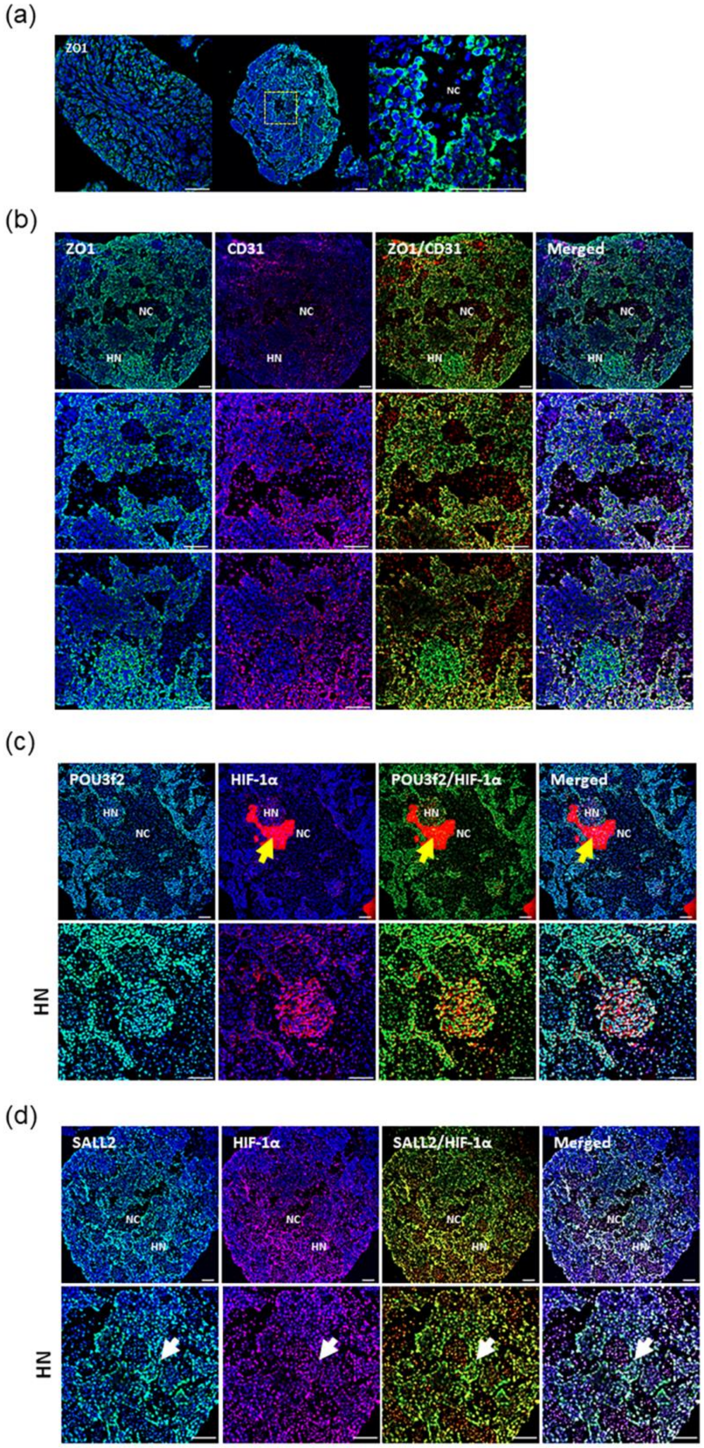

Figure 8. Spatially and hierarchically organized GSC hypoxic niche. (a)-(d) JX6 bGBO model having necrotic TME. (b)-(d) Higher magnification images of indicated regions in the bottom two rows. (a) and (b) Tight junction marker: ZO1 (green) and endothelial cell marker: CD31 (red). (c) and (d) Dedifferentiation factor: POU3f2 (green), and hypoxic marker: HIF-1α (red). (c) Yellow arrows indicate bubble between sample and the cover slide. (d) Transcription factor: SALL2 (green). White arrows indicate the potential hypoxic niche. (a)-(d) Nuclei (blue). NC: necrotic core, HN: hypoxic niche, and PVN: perivascular niche. Scale bar: 100 µm.

Figure 9

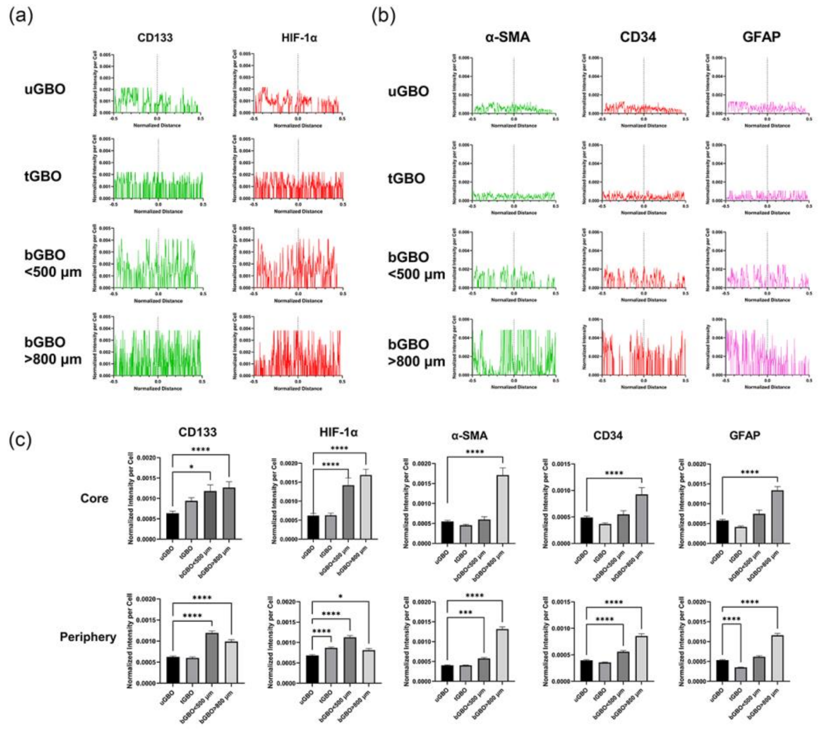

Figure 9. Quantification and comparison of the TME in JX6 PDX GBOs. (a), (b) Normalized fluorescent intensity of target protein per cell as a function of position (i.e., normalized radial distance) of an intensity profile vector spanning the whole diameter of uGBO, tGBO, bGBO<500 µm, and bGBO>800 µm. (a) GSC marker: CD133 (green) and hypoxic marker: HIF-1α (red) for size-dependent heterogeneous GSC niche. (b) Pericyte marker: α-SMA (green), endothelial cell marker: CD34 (red), and astrocyte marker: GFAP (magenta) for transdifferentiated GBM cells.

(c) Normalized fluorescent intensity of markers vs. uGBO, tGBO, bGBO<500 μm, and bGBO>800 μm in the core (top row) and the periphery (bottom row) of each GBO sample stained for GSC marker: CD133, hypoxic marker: HIF-1α, pericyte marker: α-SMA, endothelial cell marker: CD34, and astrocyte marker: GFAP. uGBO: GBOs produced from U-bottom well plates. tGBO: GBOs produced from static tissue culture flasks. bGBO: GBOs produced from bioreactors. All data presented as mean ± SE. *$p<0.05$, ***$p<0.001$, ****$p<0.0001$

Table 1. Characteristics of bioreactor vessel geometry and media. Vessel geometries and impeller diameters of two different small-scale bioreactors (BR) were measured in SI units.

Parameters	**BR1**	**BR2**
b (cm)	1.5	2.5
C (cm)	1	1
D (cm)	6	6.5
d (cm)	4	5
D/d	1.5	1.3
n_B	0	0
n_p	2	2
ρ (kg/m^3)	1008	
υ (m^2/s)	8.43 x 10^{-7}	

Table 2. Parameters for the bioreactor culture. Bioreactor culture conditions are presented in SI units. Modified Reynold's number (Re_G), power number (N_{P0}), power input (P), dissipated for power mass (ε), tip speed (υ_{tip}), eddies length (λ), and maximum shear stress ($\tau_{\max}$) were calculated in SI units using Kamei correlation (Furukawa et al., 2012).

Parameters	**BR1: *D/d* 1.5**		**BR2: *D/d* 1.3**	
V_W (mL)	60	125	60	60
H (cm)	3	5	2.5	2.5
C/H	0.33	0.2	0.4	0.4
N (rpm)	60	120	60	120
Re_G	816.14	1632.29	792.68	1585.37
N_{P0}	0.68	0.88	0.36	0.28
P (W)	6.98×10^{-5}	7.27×10^{-5}	1.14×10^{-4}	7.06×10^{-4}
P/V_L (W m^{-3})	1.55	5.81	1.91	11.77
ε (m^2 s^{-3})	1.15×10^{-3}	5.77×10^{-3}	1.89×10^{-3}	1.17×10^{-2}
υ_{tip} (m s^{-1})	0.13	0.25	0.16	0.31
λ (μm)	26.80	17.92	23.68	15.02
$\tau_{\max}$ (Pa)	0.19	0.38	0.21	0.53